THESIS FOR THE DEGREE OF LICENTIATE OF ENGINEERING

Dissipative Kerr solitons in normal dispersion microresonators

Óskar Bjarki Helgason

CHALMERS

Photonics Laboratory
Department of Microtechnology and Nanoscience (MC2)
Chalmers University of Technology
Göteborg, Sweden, 2020

Dissipative Kerr solitons in normal dispersion microresonators

Óskar Bjarki Helgason

ISSN 1652-0769
Technical Report MC2-443

Photonics Laboratory
Department of Microtechnology and Nanoscience (MC2)
Chalmers University of Technology
SE–412 96 Göteborg
Sweden
Telephone: +46 (0)31–772 10 00

Printed in Sweden by
Reproservice
Chalmers Tekniska Högskola
Göteborg, Sweden, 2020

Dissipative Kerr solitons in normal dispersion microresonators

Óskar Bjarki Helgason
Photonics Laboratory
Department of Microtechnology and Nanoscience (MC2)
Chalmers University of Technology

Abstract

The microresonator comb (microcomb) is a laser source which generates equally spaced coherent lines in the spectral domain. Having a miniature footprint and the potential of being low cost, it has attracted attention in multiple applications. Demonstrations have included high-speed optical communications, light detection and ranging, calibrating spectrographs for exoplanet detection and optical clocks. These experiments relied on the generation of dissipative Kerr solitons (DKS) which circulate in the microresonator. The development of such waveforms is paramount for further advancement of the micrcomb.

This thesis studies the dynamics of DKS in microresonators aiming at developing a low-cost, reliable and high-performing microcomb source. The investigation will cover both dark and bright DKS's, which are found respectively in normal and anomalous dispersion microresonators. The dark DKS will be in center focus since it can provide a relatively high comb power compared to other waveforms. The performance of microcombs in terms of line power is numerically explored for telecommunication purposes. The initiation of dark DKS from linearly coupled microcavities is investigated, showing efficient, low-power generation from silicon nitride microresonators that are reproducible in fabrication. These studies could facilitate reliable, low-powered, energy-efficient microcombs.

Keywords: nonlinear optics, four-wave mixing, dissipative solitons, microresonators, optical frequency combs

Publications

This thesis is based on the work contained in the following papers:

[A] Ó. B. Helgason, A. Fülöp, J. Schröder, P. A. Andrekson, A. M. Weiner and V. Torres-Company, "Superchannel engineering of microcombs for optical communications", *Journal of the Optical Society of America B*, 36, 8, 2013-2022, 2019.

[B] E. Nazemosadat, A. Fülöp, Ó. B. Helgason, P.-H. Wang, Y. Xuan, D. E. Leaird, M. Qi, E. Silvestre, A. M. Weiner and V. Torres-Company, "Switching dynamics of dark-pulse Kerr comb states in optical microresonators", *arXiv*:1910.11035, 2019.

[C] Ó. B. Helgason, F. R. Arteaga-Sierra, Z. Ye, K. Twayana, P. A. Andrekson, M. Karlsson, J. Schröder and V. Torres-Company, "Dissipative Kerr solitons in photonic molecules", *arXiv*:2007.02608, 2020.

Related publications and conference contributions by the author, not included in the thesis):

[D] D. Kong, A. A. Jørgensen, M. R. Henriksen, F. Klejs, Z. Ye, Ò. B. Helgason, H. E. Hansen, H. Hu, M. Yankov, S. Forchhammer, P. Andrekson, A. Larsson, M. Karlsson, J. Schröder, Y. Sasaki, K. Aikawa, J. W. Thomsen, T. Morioka, M. Galili, V. Torres-Company, and L. K. Oxenløwe "Single Dark-Pulse Kerr Comb Supporting 1.84 Pbit/s Transmission over 37-Core Fiber", *Conference on Lasers and Electro-Optics (CLEO)*, San Jose, USA, paper JTh4A.7, 2020.

[E] Ó. B. Helgason, Z. Ye, K. Twayana, P. A. Andrekson, J. Schröder and V. Torres-Company "Dark-pulse Kerr combs in linearly coupled microring structures", *Conference on Lasers and Electro-Optics (CLEO)*, San Jose, USA, paper STu3H.5, 2020.

[F] V. Torres-Company, J. Schröder, A. Fülöp, M. Mazur, L. Lundberg, Ó. B. Helgason, M. Karlsson and P. A. Andrekson "Laser Frequency Combs for Coherent Optical Communications", *Journal of Lightwave Technology*, **37**, 7, 1663-1670, 2019.

[G] Z. Ye, A. Fülöp, Ó. B. Helgason, P. A. Andrekson, and V. Torres-Company "Low-loss high-Q silicon-rich silicon nitride microresonators for Kerr nonlinear optics", *Optics Letters*, **44**, 3326-3329, 2019.

[H] A. Fülöp, M. Mazur, A. Lorences-Riesgo, Ó. B. Helgason, P.-H. Wang, Y. Xuan, D. E. Leaird, M. Qi, P. A. Andrekson, A. M. Weiner and V. Torres-Company "Low-loss high-Q silicon-rich silicon nitride microresonators for Kerr nonlinear optics", *Nature Communications*, **9**, 1598, 2018.

[I] E. Nazemosadat, A. Fülöp, Ó. B. Helgason, P.-H. Wang, Y. Xuan, D. E. Leaird, M. Qi, E. Silvestre, A. M. Weiner, and V. Torres-Company "Hot-Cavity Spectroscopy of Dark Pulse Kerr Combs in Microresonators", *Conference on Lasers and Electro-Optics Europe & European Quantum Electronics Conference (CLEO/Europe-EQEC)*, Munich, Germany, paper ed65, 2019.

[J] E. Nazemosadat, A. Fülöp, Ó. B. Helgason, P.-H. Wang, Y. Xuan, D. E. Leaird, M. Qi, E. Silvestre, A. M. Weiner, and V. Torres-Company "Switching Dynamics of Dark Solitons in Kerr Microresonators", *Conference on Lasers and Electro-Optics Europe & European Quantum Electronics Conference (CLEO/Europe-EQEC)*, Munich, Germany, paper ef84, 2019.

[K] Z. Ye, A. Fülöp, Ó. B. Helgason, P. A. Andrekson, V. Torres-Company "Low loss silicon-rich silicon nitride for nonlinear optics", *Conference on Lasers and Electro-Optics (CLEO)*, San Jose, USA, 2018

[L] Ó. B. Helgason, A. Fülöp, J. Schröder, P. A. Andrekson, A. M. Weiner, V. Torres-Company "Superchannel engineering with microresonator combs", *Conference on Lasers and Electro-Optics (CLEO)*, San Jose, USA, 2018

Contents

Acknowledgement

First, I would like to thank my supervisor, Associate Professor Victor Torres-Company, for giving me the opportunity to study towards a PhD, and for helping me through it thus far. I am grateful to Dr. Jochen Schröder for valuable support and guidance. I also thank Prof. Peter Andrekson and Prof. Magnus Karlsson for sharing helpful knowledge and insights.

The Ultrafast Photonics Laboratory consists of wonderful people that I thoroughly enjoy working with. I am thankful to all of them for how ready they have been to help and discuss things over the years. I am especially grateful to Dr. Attila Fülöp for giving up so much of his time to teach me about microcombs and laboratory work. I thank Zhichao Ye for fruitful discussions and for making excellent microrings that have boosted the value of my research. I appreciate having a great office mate and a soliton expert in Dr. Fransisco Arteaga-Sierra. I thank Marcello Girardi for enduring countless excessively long conversations with me about microcombs and other topics.

I would like to thank everyone in the Photonics Laboratory for all the help and fun I have had with them. I have been lucky to have enjoyed the friendship of Alexander Grabowski through the master studies and now as I do the PhD. I am also thankful for the help I got from Dr. Lars Lundberg, Dr. Mikael Mazur and Dr. Benjamin Foo in the first couple of years of my PhD.

Finally, I would like to thank all my friends and family for their incredible support throughout the years. Most importantly, thank you Þórdís, Sigurlaug and Andrea for putting up with me through all of this.

Acronyms

CMOS	complementary metal–oxide–semiconductor
CW	continuous wave
DS	dissipative soliton
DKS	dissipative Kerr soliton
EOC	electro-optic comb
FSR	free spectral range
FWHM	full width at half maximum
FWM	four-wave mixing
GVD	group velocity dispersion
LLE	Lugiato-Lefever equation
MI	modulation instability
Microcomb	microresonator frequency comb
MLL	mode-locked laser
NLSE	nonlinear Schrödinger equation
OFC	optical frequency comb
RF	radio frequency
SPM	self-phase modulation
XPM	cross-phase modulation

Chapter 1

Introduction

In 2005, John L. Hall and Theodore W. Hänsch shared half of the Nobel prize in physics for their contributions to precision spectroscopy [1, 2]. Their work in the late 90s and early 2000s would lead to dramatic improvements to atomic clocks [3,4], but a key element to their success was the development of an optical frequency comb (OFC).

In contrast to the continuous wave (CW) laser, which outputs light at a single discrete frequency, an OFC is a laser source that outputs a series of equally spaced lines in the frequency domain [5]. A critical feature of these comb lines is that they are phase-locked to each other. As such, they typically correspond to a train of optical pulses in the time domain, with a repetition rate (f_{rep}) equal to the comb line separation. The absolute optical frequency of each comb line (f_n) is represented by $f_n = nf_{rep} + f_{ceo}$, where f_{ceo} stands for carrier-envelope offset frequency, caused by a constant phase slippage between consecutive pulses. Thus, the absolute frequency of each comb line can be determined if both f_{rep} and f_{ceo} are known.

While f_{rep} is usually easily measured as a radio frequency (RF) beatnote between comb lines, measuring f_{ceo} comprises a massive challenge, which was one of the main achievement of the Nobel awarded OFC. It required an octave-spanning comb spectrum, accomplished by broadening a mode-locked laser (MLL) via the Kerr effect in a highly nonlinear fiber (HNLF). By implementing a self-referencing technique, the f_{ceo} of the octave-spanning comb was made available as an RF beatnote [6] such that the absolute frequency of each comb line could be determined and stabilized with remarkable precision. Utilizing the comb lines as a series of optical references, this enabled the determination of optical frequencies

with orders of magnitude higher precision and lower hardware complexity compared to previous technologies, facilitating the development of optical clocks [7].

The research field of OFCs has since expanded at an incredible rate. OFCs are now studied within multiple application domains, e.g. as an astrocomb [8], where a spectrograph calibrated with an OFC captures the Doppler shift of stars for exoplanet detection; for dual-comb spectroscopy [9], a technique useful both for spectroscopy and light detection and ranging (LIDAR) where two OFC combs are used to map an optical spectrum onto a narrower RF spectrum; in RF photonics [10], e.g. to generate low noise microwave signals; and in optical telecommunications [11], replacing multiple CW lasers for carrier generation and enabling other enhancements in terms of spectral efficiency and signal processing. Note that the need for self-referencing, and the optimal comb characteristics in general, varies on a case by case basis. For example, atomic clocks require self-referencing with high stability and an octave-spanning spectrum [6]. In contrast, optical telecommunications require a relatively narrow and flat spectrum with high line power compared to the surrounding optical noise power (i.e. high optical signal to noise ratio) [12].

Different sources can be employed as an OFC. One is the MLL, which generates synchronized optical pulses by periodically introducing absorption to a laser cavity, where the line spacing of the generated OFC is defined by the length of the laser cavity [13]. Having existed since the early 60's [14], the MLL is a well established and commercially available OFC source. The electro-optic comb (EOC) is another OFC source, which is easily assembled using commercially available components primarily developed for telecommunications. It is generated by modulating a CW laser with an RF tone via electro-optic modulation (EOM), typically using a cascade of phase and intensity modulators [15]. It is flexible in terms of tunability since the center frequency can be changed by tuning the wavelength of the laser and the line spacing can be changed by tuning the frequency of the RF tone. The spectrum can be broadened to an octave in a highly nonlinear fiber, but an excess of phase noise originating in the RF clock is often an obstacle to self-referencing. Recent experiments have overcome this obstacle by filtering the lines of the EOC in an optical cavity, achieving self-referencing at a stability comparable to the MLL [16, 17].

With the MLL and the EOC readily available as table-top solutions,

an increasing effort has been spent on realizing chip-scale OFCs. Such devices promise a dramatic reduction in size with co-integration of other optical components at a potential low cost, e.g. using fabrication methods compatible with complementary metal–oxide–semiconductor (CMOS) processes [18]. Miniaturization opens new opportunities, especially in settings outside of the laboratory. While progress has been made in making chip-scale MLLs [19] and EOCs [20], another prominent candidate is the microresonator frequency comb (microcomb) [21, 22].

First demonstrated in the mid 2000s [23], the microcomb is generated in a microresonator by employing the Kerr effect to convert input power from a CW laser to other comb lines [24]. The generated lines are confined to the resonances of the cavity, where four-wave mixing (FWM) allows energy transfer to evenly spaced and coherent comb lines. A thorough investigation of the nonlinear microcavity physics has led to the realization of coherent microcombs exhibiting several distinct intracavity waveforms in the form of dissipative Kerr solitons (DKS). Among those are the heavily researched bright DKS [25] and soliton crystals [26], both found in anomalous dispersion cavities, but also the less known dark DKS (sometimes called mode-locked dark pulse), found in normal dispersion cavities [27]. Such waveforms have been used for microcomb demonstrations in applications [21], ranging from optical clocks [28] to optical telecommunication [29, 30].

Further studies into the dynamics of the DKS have led to promising designs towards reliable comb generation [31–33]. Microcombs using less than a milliwatt of CW laser power have been demonstrated [34]. Such low power operation is in the domain of integrated lasers, which enables further miniaturization of the comb source [35, 36]. Promising as these experiments were, the microcomb still requires more development to be established as a competing OFC solution. One persisting challenge is limited conversion efficiency, i.e. the portion of input optical CW power converted to comb lines at other frequencies. Having low power conversion efficiency translates into lower wall-plug energy efficiency and low optical signal to noise ratio. This is especially true for the bright DKS, where the conversion efficiency is fundamentally limited [37]. The DKS's generated in the normal dispersion regime offers much higher conversion efficiency but at the cost of a more uneven spectrum [38]. A further study into the dynamics and designs of these waveforms is essential for the realization of reliable, energy-efficient microcombs.

1.1 This thesis

This thesis focuses on the dynamics of microresonator frequency combs with the overall goal of realizing reliable designs with high conversion efficiency and flat spectral distribution of power. These characteristics are especially appealing to optical telecommunications. Thus, more emphasis will be put on dark DKS since they offer much higher conversion efficiency compared to the bright DKS.

In Paper A, single-mode microresonators are studied, where both bright and dark DKS are numerically simulated over a large parameter space in order to discover optimized designs for optical telecommunication applications.

Paper B features a careful experimental and numerical investigation of the initiation process of dark DKS's from a CW laser in a single microcavity containing two linearly coupled transverse modes.

In Paper C, microcombs are experimentally demonstrated from two linearly coupled normal-dispersion microresonators. Numerical simulations show that these microcombs exhibit temporal waveform with characteristics similar to a dark DKS. The existence regime of these microcombs is found considerably larger compared to dark DKS from a single-mode cavity operation.

1.1.1 Thesis outline

This thesis is organized as follows: Chapter 2 serves as a brief introduction to the soliton dynamics of nonlinear waveguides. Chapter 3 discusses the cold cavity dynamics of microresonators, both for single microcavities and linearly coupled cavities. In Chapter 4, the microcomb generation and soliton dynamics in microcavities are described. Finally, Chapter 5 is the future outlook.

Chapter 2

Dynamics in nonlinear waveguides

An essential part of microcomb generation is the circulation of light through a nonlinear waveguide. This propagation is ruled by the Kerr effect and dispersion, similar to the optical fiber, which can be modeled with the nonlinear Schrödinger equation (NLSE). The NLSE predicts the existence of solitons in optical fibers [39], and with the right modifications, it can be used to predict dissipative solitons in microresonators. In the next section, the NLSE will be briefly introduced. It is then employed in the second section to describe the basic dynamics of solitons with particular focus on dissipative solitons.

2.1 The nonlinear Schrödinger equation

An optical field propagating in a waveguide is governed by Maxwell's equations. Propagating in the z-direction, the field is described by its transverse modes. For all work in this thesis we can ignore the z-component of the electric field and consider a single polarization. The NLSE is an approximation of the evolution of a slowly varying electric field envelope (A) in a single transverse mode as it propagates in a single direction through a waveguide featuring the Kerr effect. It presents the characteristics of the transverse modes as constants (e.g. loss, dispersion, nonlinearity) that modify the electric field envelope as a scalar as it moves in the z-direction. Details about the derivation can be found in the literature [40]. The NLSE is given by

$$\frac{\partial A}{\partial z} = i\gamma|A|^2 A - \frac{\alpha}{2}A - \beta_1\frac{\partial A}{\partial t} - \frac{i\beta_2}{2}\frac{\partial^2 A}{\partial t^2} + \frac{i\beta_3}{6}\frac{\partial^3 A}{\partial t^3}, \tag{2.1}$$

where α is the propagation loss for each unit of length, β_1 is the inverted group velocity, and β_3 is the third-order dispersion (TOD). The group velocity dispersion (GVD) is described by β_2, where anomalous dispersion ($\beta < 0$) signifies that higher frequencies go faster than lower frequencies, while normal dispersion ($\beta > 0$) signifies the opposite. The Kerr effect is depicted by the nonlinear coefficient, γ, which can manifest in several nonlinear effects, such as self-phase modulation (SPM), cross-phase modulation (XPM), and four-wave mixing (FWM). Here, the electric field envelope is normalized such that $|A|^2 = P$, where P is the optical power. The normalized electric field can be found as

$$E(z,t) = A(z,t)e^{i(\beta_0 z - \omega_0 t)} \tag{2.2}$$

where β_0 is the wavenumber.

Because of the nonlinear term, the NLSE is not easy to analytically integrate. However, it is relatively simple to simulate. The simulations in this work will be based on either the split-step method [40] or the Runge-Kutta method in the interaction picture [41], but both methods simulate propagation by taking small enough steps such that the nonlinear and linear portion of the NLSE can be applied separately. For simplification, the β_1 is often removed from the equation by assuming a reference frame moving at the speed of group velocity.

2.2 Introduction to soliton dynamics

Solitons were first discovered as translational waves in a water canal by J.S. Russell in the early 1800s [42]. It is defined as a wave that travels through time and space at a constant velocity while maintaining its shape [43]. They are found in energy conservative systems, arising as a balance between dispersive elements and nonlinearities.

Found in multiple domains of physics, solitons were first described in optical fibers in 1973 [44], with bright solitons appearing in the anomalous dispersion regime and dark solitons in the normal dispersion regime. Examples of a split-step simulation in an optical fiber only featuring the Kerr nonlinearity and GVD are displayed in Figure. 2.1, initiating the solitons from mathematical closed-form expression [40]. These propagate unchanged because of a balance between the GVD and SPM. The source

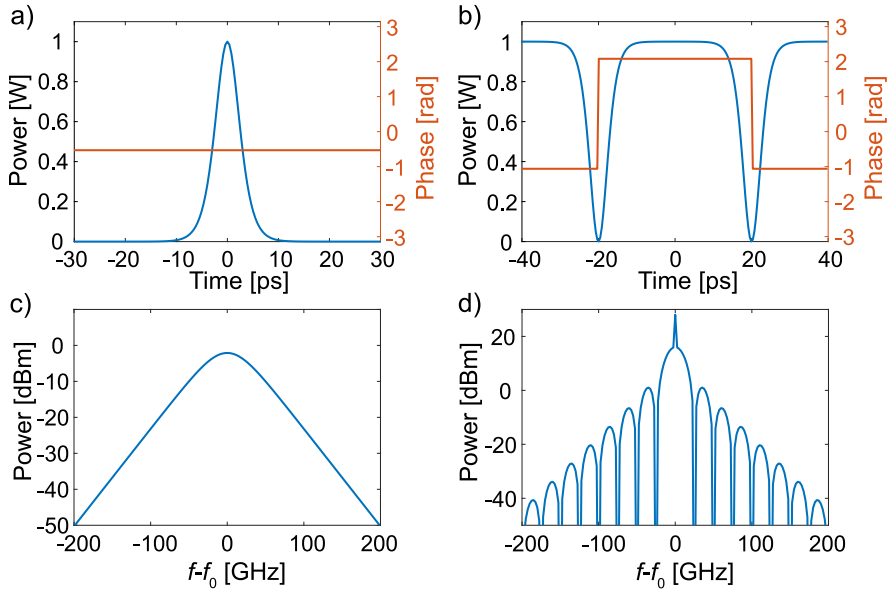

Figure 2.1: The plot in a (b) shows the temporal feature of single bright (two dark) soliton after 100 km lossless propagation in an optical fiber, i.e. the pulse is only affected by the Kerr effect and GVD ($\gamma = 0.002\,(Wm)^{-1}$, $\beta_2 = \pm 20\,ps^2/km$). The corresponding spectrum is shown in c and d for bright and dark solitons respectively. The simulations showed that these waveforms would propagate without change to temporal and spectral power profiles. Note that the bright soliton features a constant phase, while the dark solitons exhibit a π phase shift. Two dark solitons are simulated to avoid simulation artifacts.

of this balance is that the self-phase modulation generates a positive chirp in a negative slope of the intensity distributed pulse and a negative chirp in the positive slope of a pulse. For the bright soliton, this means that lower frequencies will appear on the leading edge, but the anomalous GVD corrects this chirp since the higher frequencies move faster. A similar story can be told about the dark soliton, only with higher frequencies appearing on the trailing edge.

In a lossless fiber, a soliton can propagate indefinitely. It was for this reason that much effort was spent on using solitons for carrying data in fiber optical communications [39]. However, losses of the fiber become significant at longer distances, causing the soliton to become wider and shrink in amplitude [45]. Systems involving various gain elements were often deployed such that the average system would be effectively lossless

while maintaining similar soliton dynamics. However, many amplified systems can support soliton-like dynamics that are distinctly different from the fiber soliton. These are dissipative solitons, discussed in the next section.

2.3 Dissipative solitons

Much like solitons found in conservative systems, dissipative solitons (DS) rely on a balance between nonlinearity and dispersion. The main difference is that the DS thrive in systems with continuous energy exchange, where the DS existence also depends on the balance between gain and loss [46]. They are found in a wide range of optical systems, one of which is the Mode-locked laser (MLL).

The DS generated in an MLL generally appears as a balance between the GVD, Kerr nonlinearity, amplification and cavity losses. The MLL features amplification in a resonant cavity, often with other added elements such as spectral filters, saturable absorbers and a Kerr medium. As such, a wide range of MLL configurations is possible, enabling a variety of DS dynamics [47]. Not only does this include bright and dark DS waveforms that are similar to the fiber solitons [48,49], but also different shapes such as flat-top pulses and composite pulses [50–52].

Optical resonant cavities can also maintain a DS when excited by a laser [53], e.g. DS's in microresonators. The gain of a microcomb DS is usually supplied via parametric amplification of a CW input pump over a broad spectrum which compensates for the losses [21]. This employment of the Kerr effect to supply gain is perhaps the reason why these waveforms have become known as dissipative Kerr solitons (DKS). As such, the power of the center wavelength needs to be kept at a high enough level so that it can maintain the DKS.

The dynamics of DKS are not only captured by microresonators. An MLL cavity can support a DKS through saturated amplification of the center wavelength of the DKS. Figure 2.1a shows the layout of a simple cavity with such an amplifier, where the gain profile does not reach other resonant modes of the cavities. A simulation was conducted by solving equation 2.1 ($\beta_2 = \pm 200\ ps^2/km$, $\gamma = 0.002(Wm)^{-1}$, $\alpha = 0.9\ km^{-1}$) for a full roundtrip of propagation ($L = 20\ cm$). In each roundtrip, a portion of power was coupled from the cavity ($\theta = 0.002$) and the amplifier would amplify according to $A'(f_0) = A(f_0)e^{P_{sat}\frac{\alpha L+\theta}{P_{sat}+|A(f_0)|^2}}$. Figures 2.1b-d show the generation of a dark DKS in the normal dispersion re-

gion, with $P_{sat} = 7.4W$, initiating from two dark solitons similar to figure 2.1b. Figures 2.1e-g. The bright DKS is displayed, with $P_{sat} = 1.5\,W$, and initiating from a bright soliton similar to figure 2.1a. For the soliton to stabilize, a constant delay of 0.0017 radians to the center wavelength was needed every roundtrip. The resulting waveforms are distinctly different from the fiber solitons in Figure. 2.1, both in phase and amplitude. This is particularly noticeable in the normal dispersion regime, which exhibits a single dark DKS without the π phase shift characteristic to dark solitons in fibers. This goes to show that the dynamics of DKS cannot be accurately depicted by the physics of typical fiber solitons.

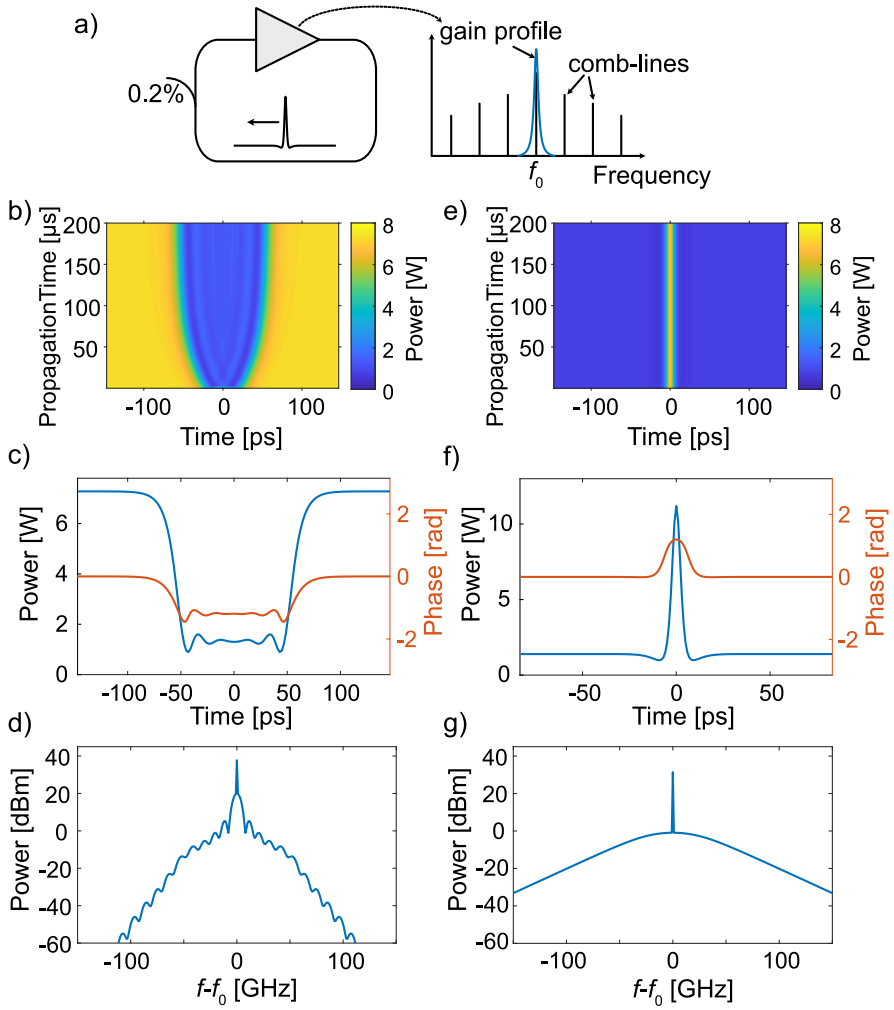

Figure 2.2: a) shows a layout of a laser cavity which can be used to generate a DKS. b) shows the evolution of a dark DKS from initiation, c) shows the temporal features and d) shows the spectrum. e) shows the evolution of a bright DKS from initiation, f) shows the temporal features and g) shows the spectrum.

Chapter 3

Cold cavity dynamics of microresonators

Microresonators are optical cavities that typically have a sub-millimeter footprint. Like most other resonators, their operation is based on constructive interference, allowing them to store energy for wavelengths of light that are an integer multiple of the cavity length. Thus, light at these selected wavelengths is allowed to couple into the microcavity where it builds up in power, while other wavelengths are rejected. As such they are found in multiple applications, such as dynamic filters and laser cavities [54, 55].

The main aim of this chapter is to introduce the dynamics and characteristics of microresonators when nonlinearities are negligible, aiming at cavities that enable microcomb generation. While this study focuses on integrated microring resonators in silicon nitride, it will in most cases apply to optical resonators in general. The next section will cover the dynamics of one microring supporting a single transverse mode, i.e. the dynamics that enable the DKS's in Paper A. The second section will introduce linearly-coupled transverse modes, which involve the dynamics that enabled DKS generation in Paper B. The third section discusses the dynamics of linearly coupled rings, which were employed for generating DKS in Paper C.

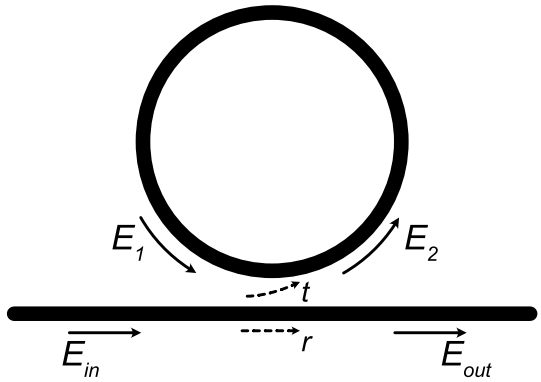

Figure 3.1: A basic layout of the microring resonator: A bus waveguide coupled to a ring waveguide.

3.1 The linear frequency response of a single-mode microresonator

A typical microring resonator features a bus waveguide and a ring waveguide placed in close proximity (see Figure 3.1). The distance is short enough such that the edges of the mode profiles in both waveguides overlap, such that one mode induces a weak perturbation to the other. This leads to periodic exchange of power between the two waveguides [56]. Assuming weak coupling over a short distance of interaction, the coupling is approximated to occur in a single point [57] using the following coupling matrix:

$$\begin{bmatrix} E_{out} \\ E_2 \end{bmatrix} = \begin{bmatrix} r & it \\ it & r \end{bmatrix} \begin{bmatrix} E_{in} \\ E_1 \end{bmatrix}, \tag{3.1}$$

where t and r represent the coupling coefficients between the electric fields as depicted in figure 3.1. The coupler is assumed to be lossless, such that $1 = r^2 + t^2$. In addition, the propagation over a full roundtrip in the ring (when nonlinearity is neglected) is described by

$$\frac{\partial E}{\partial z} = -\frac{\alpha}{2}E + i\beta(\Delta\omega)E \tag{3.2}$$

where α is the propagation loss, $\beta(\Delta\omega) = \beta_0 + \beta_1\Delta\omega + \beta_2/2(\Delta\omega)^2 + \cdots$ is the frequency dependent propagation constant expanded around the

center frequency ω_0, ω is the angular frequency and $\Delta\omega = \omega - \omega_0$. This equation can be solved as

$$E_1 = E_2 e^{(-\alpha/2 + i\beta(\Delta\omega))L}, \tag{3.3}$$

where L is the roundtrip length of the ring.

The system of equations formed by equation 3.1 and equation 3.3 describes the linear response of the microring. Using these equations, the power transmission can be derived as [58, 59]

$$T(\Delta\omega) = \frac{|E_{out}(\Delta\omega)|^2}{|E_{in}(\Delta\omega)|^2} = \frac{a^2 - 2ra\cos(\beta(\Delta\omega)L) + r^2}{1 - 2ra\cos(\beta(\Delta\omega)L) + (ra)^2}. \tag{3.4}$$

This equation is especially useful for the characterization of microresonator devices since such transmission is easily measured by scanning the frequency of an input laser while recording the output power in a photodiode. It describes the appearance of resonances separated by the FSR which has a frequency dependence in the presence of the GVD and higher-order dispersion. The locations of the resonance center is described by $\beta(\Delta\omega)L = 2\pi\mu$, where μ is the longitudinal mode number (see figure 3.2a-b). Thus, the resonances appearing in a transmission scan can be used to determine the dispersion profile of the resonator waveguide (see figure 3.2c).

Not only are the resonances defined by the dispersion profile, but they are also influenced by the cavity losses, i.e. both intrinsic losses (a) and coupling losses (r). The impact of the losses is seen in the full width at half maximum (ω_{FWHM}) and depth (described by R) of the resonance (see figure 3.2 c). For the purpose of analysing these characteristics, it is useful to approximate the cosine term of equation 3.4 with $\cos(x) \approx 1 - x^2/2$, which holds fairly well when cavity losses are low. The result is a Lorentzian shaped function

$$T = \frac{(\beta L)^2 + R(\Gamma/2)^2}{(\beta L)^2 + (\Gamma/2)^2}, \tag{3.5}$$

$$R = \frac{(r-a)^2}{(1-ra)^2} \quad , \quad \Gamma = 2\frac{(1-ra)}{\sqrt{ra}} = \frac{\omega_{FWHM}\omega_{FSR}}{2\pi}. \tag{3.6}$$

With prior knowledge of the FSR, finding the FWHM and resonance depth of a resonance is enough to determine the values of the intrinsic and extrinsic loss parameters, a and r. Note however that a and r are tangled

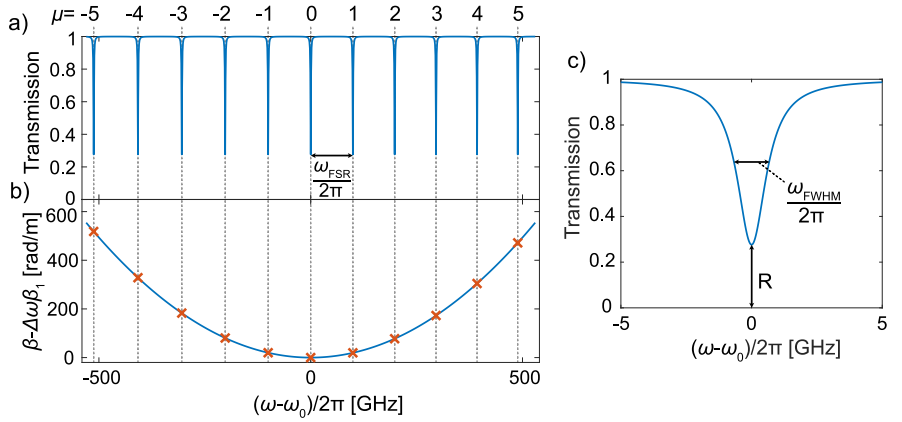

Figure 3.2: a) shows a microring transmission spectrum according to equation 3.4, using parameters $a = 0.99$, $r = 0.968$, $\beta_0 = 0$, $\beta_1 = 6.67\, ps/km$, $\beta_2 = 100000\, ps^2/km$ and $L = 1.5\, mm$. The GVD causes the FSR to change with frequency, which means that the mode numbers are not appearing at equally spaced frequencies. The GVD is rather exaggerated such that this uneven separation becomes noticeable. b) shows the variation in propagation constant with frequency, with effects of β_1 subtracted. It shows clearly the positive parabolic curve caused by the normal GVD term, but this curve becomes negative when anomalous dispersion is considered. The red markings corresponding to the location of the resonances. c) shows a closer look at one of the resonances, displaying FWHM and resonance depth.

in the equations, such that it is not possible to tell if the resonance is undercoupled ($r > a$) or overcoupled ($r < a$). This could be determined from the phase profile of the resonance, for which a coherent detection is required [58]. In practice, when there is a large difference between a and r, this can be determined from prior knowledge of the design. The latter approach was used when characterizing the microrings in Paper B and C.

The losses of resonator cavities are commonly represented by the quality factor (Q), which describes the number of optical cycles experienced by an optical field in the resonator cavity before the intrinsic and extrinsic losses reduce its energy by a factor 1/e. It relates to a resonance shape through

$$\mathrm{Q} = \frac{\omega_0}{\omega_{FWHM}} \approx \frac{\omega_0 n_g L \sqrt{ra}}{\pi(1-ra)c_0}, \tag{3.7}$$

which makes it easily definable from a resonance profile. The quality factor is often described as a combination between the extrinsic and intrinsic quality factors (Q_i and Q_e). Assuming low intrinsic and extrinsic losses, these can be approximated as

$$Q^{-1} \approx Q_i^{-1} + Q_e^{-1}, \tag{3.8}$$

$$Q_i \approx \frac{\omega_0 n_g L\sqrt{a}}{\pi(1-a)c_0} \quad , \quad Q_e \approx \frac{\omega_0 n_g L\sqrt{r}}{\pi(1-r)c_0}. \tag{3.9}$$

The quality factor carries much significance when it comes to build up of power in the microcavity. Such buildup of power is essential for microcombs, since they operate through the Kerr effect. The power buildup factor at center of resonance can be found as [59]

$$\frac{|E_1(\Delta\omega)|^2}{|E_{in}(\Delta\omega)|^2} = \frac{(1-r^2)a^2}{(1-ra)^2} \propto \frac{aQ^2}{r}. \tag{3.10}$$

Assuming that both intrinsic and extrinsic losses are low ($r, a \approx 1$), the buildup of power in the cavity rises quadratically with the quality factor. Since the coupling rate can be managed in design, realizing microcomb operation at low power levels will ultimately be limited by the intrinsic losses. For silicon nitride microresonators, these intrinsic losses are usually dominated by scattering due sidewall roughness of the waveguides [60]. Reducing the impact of these losses [61] was an essential part of realizing the low-power microcombs in Paper C.

3.2 Dynamics of linearly coupled transverse modes

The analysis in the previous section was based on propagation in a single transverse mode in the microresonator. For microcomb generation, much focus is put on realizing waveguide dimensions with favorable Kerr coefficient and GVD, often leading to larger waveguides supporting more than one mode. While these transverse modes are orthogonal in theory, they will often exhibit perturbations due to sidewall roughness, leading to linear coupling (κ) between two transverse modes [62–64]. These effects are unwanted in general as they can prohibit or deform DKS generation [65]. However, such perturbations can be of benefit in normal GVD waveguides, as they can enable the generation of a dark DKS from

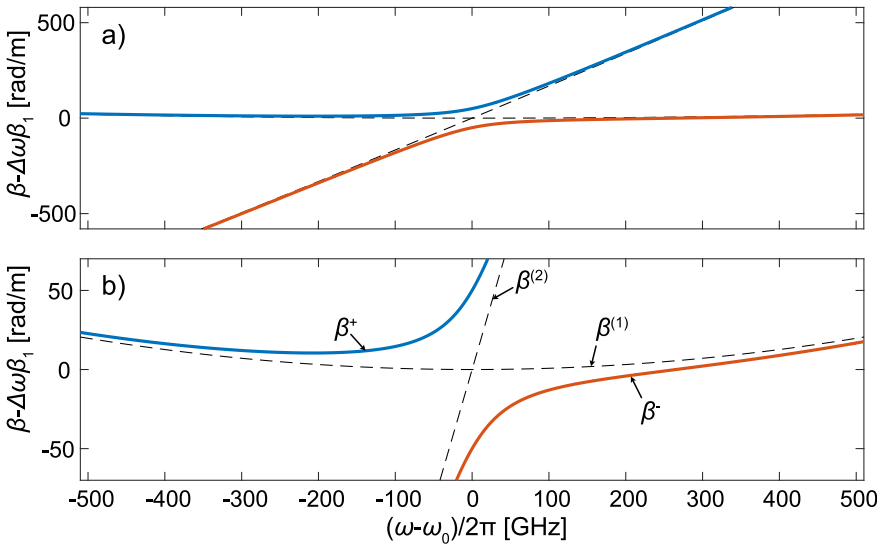

Figure 3.3: a) shows the dispersion profile of two linearly coupled modes, where b) provides a zoom-in on the y-axis. The supermodes (β^+ and β^-) and the uncoupled modes ($\beta^{(1)}$ and $\beta^{(2)}$) are marked in the figure. The parameters used were $\beta_0^{(1)} = \beta_0^{(2)} = 0$, $\beta_1^{(2)} = 1.04 \cdot \beta_1^{(1)} = 6.8\, ns/m$, $\beta_2^{(2)} = \beta_2^{(1)} = 4000\, ps^2/km$ and $\kappa = 50\, m^{-1}$.

a CW laser [27]. In fact, such a coupling was essential for the generation of the dark DKS in paper B. This section provides a brief introduction into the dynamics of such mode-coupling.

Let us consider a weak linear coupling between two co-propagating transverse modes, which can be modeled by [56, 66]

$$\begin{aligned} \frac{\partial E_1}{\partial z} &= i\zeta_1 E_1 + i\kappa E_2, \\ \frac{\partial E_2}{\partial z} &= i\kappa E_1 + i\zeta_2 E_2, \end{aligned} \tag{3.11}$$

where κ is the coupling coefficient between modes 1 and 2 and $\zeta_n = i\alpha_n/2 + \beta^{(n)}$ is the complex propagation constant of mode n. Modes 1 and 2 are considered to be a fundamental mode and higher order transverse mode, respectively. The coupling breaks the orthogonality between the modes, allowing them to exchange power in a periodic manner. However, a new basis can be found for the perturbed system with orthogonal

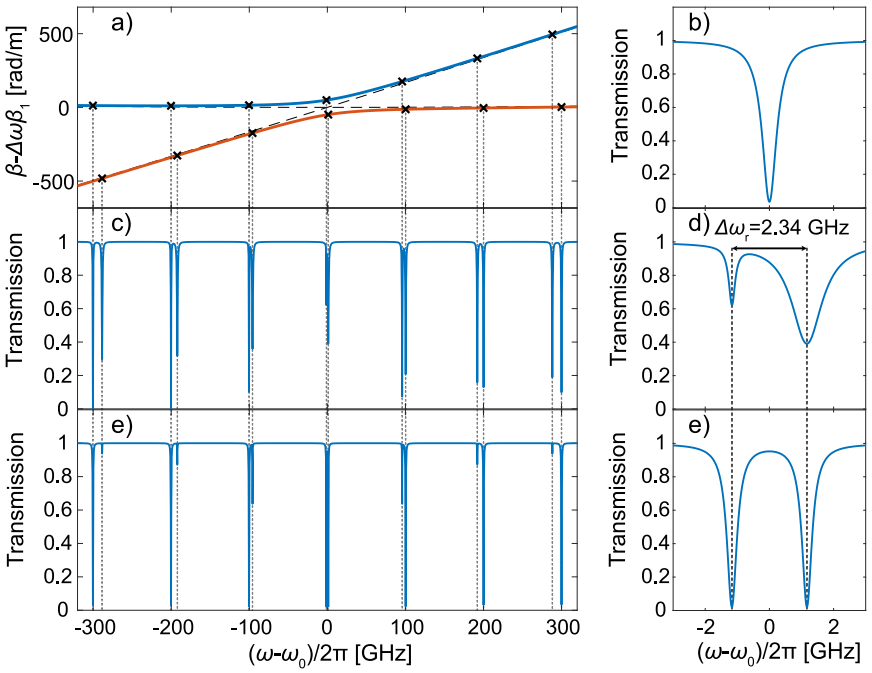

Figure 3.4: a) shows the coupled-mode dispersion profile from figure 3.3, but the figures below will have the same $\beta^{(1)}$, $\beta^{(2)}$ and κ values. b) shows a resonance profile of mode 1 with $\kappa = 0$. c) is a resonance transmission with power coupled from the bus waveguide into both modes ($\theta_1 = 0.02$, $\theta_2 = 0.04$) and with $\kappa = 50m^{-1}$. The shaded lines connect the resonances to the dispersion profile in a), indicating to which mode they belong. The resonances of the two modes are shown to shift across one another due to the difference in group velocity. d) shows a zoom-in to the center of the same resonance transmission. In contrast to the uncoupled resonance in b), the mode-coupling causes the resonances to shift off center. Finally, e) and f) show a similar response as c) and d), with $\theta_2 = 0$. The effect is that the resonances corresponding to mode 2 (seen in a) as the diagonal uncoupled mode) will disappear.

modes, called supermodes [67]. These supermodes can be written as a superposition of the orthogonal modes of the unperturbed system. The propagation constant of the supermodes can be derived from 3.11 as [56]

$$\zeta_{\pm} = \frac{\zeta_1 + \zeta_2}{2} \pm \sqrt{\left(\frac{\zeta_1 - \zeta_2}{2}\right)^2 + |\kappa|^2} \tag{3.12}$$

with an example displayed in figure 3.3a. The losses will have negligible impact and are thus not included in the example, hence ζ is replaced by β. The figure shows the dispersion profile of the modes 1 and 2, with and without linear coupling. The coupling induces a change in the dispersion profile, but it is only significant when the difference between the two propagation constants ($|\beta^{(1)} - \beta^{(2)}|$) is not significantly larger than the coupling rate (κ). The maximal separation between supermodes and uncoupled modes is reached at the mode crossing, where $\beta^{(1)} = \beta^{(2)}$. Note that even though the uncoupled modes 1 and 2 cross, the supermodes avoid each other at the crossing. It is therefore often referred to as an avoided mode-crossing. Figure 3.3b depicts the enlarged profile. Here, both uncoupled modes 1 and 2 have normal GVD, which can be seen in the upwards curving parabolic shape of mode 1. This parabolic curve is heavily modified in the presence of mode-coupling, exhibiting a downward curve for β^- which can be interpreted as localized anomalous dispersion. This feature is important as it can enable modulational instability, a process that allows the initiation of dark DKS from a CW input. This was in fact the key element that enabled the dark DKS generation in normal-dispersion linearly-coupled transverse modes from a CW laser in Paper B.

Let us consider a microresonator with the same layout as 3.1, but supporting two transverse modes: mode 1, which is the fundamental mode; and mode 2, which is a higher-order transverse mode. The transmission spectrum of a microcavity featuring the coupled modes will display resonances which can be used to characterize the cavity. However, the location of these resonances will not be defined by the uncoupled modes, but rather the supermodes as $\beta^+ L = 2\pi n$ and $\beta^- L = 2\pi m$, where n and m are integer numbers.

The response can be modeled using a system combining equation 3.11 with a coupling matrix describing a directional coupler between the bus waveguide and the two modes of the microcavity, with the model detailed in Paper B. Here, this system is numerically solved to display a transmission spectrum of the microcavity in figure 3.4. The dispersion parameters and coupling are the same as in figure 3.3, with $\alpha_1 = \alpha_2 = 9.2\,m^{-1}$ and the power coupling ratio to mode 1 and 2 is $\theta_1 = 0.02$ and $\theta_2 = 0.04$. The resulting transmission spectrum is displayed in figure 3.4 c-d. It shows resonances whose locations are described by the dispersion profile in figure 3.3. Far away from the mode crossing, the resonances of the transverse modes are not impacted by the mode coupling. These

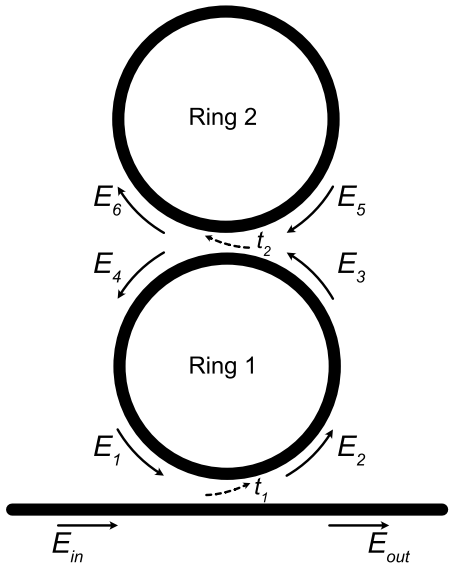

Figure 3.5: A basic layout of two linearly coupled microrings

can be used to characterize the transverse modes separately using the single-mode model from section 3.1 to retrieve the dispersion and losses. The coupling coefficient can then be derived by a measured fitting of the resonances near the avoided mode crossing with equation 3.11. Alternatively, in the special case when $\beta^{(1)} = \beta^{(2)}$ as is the case for the resonances displayed in figure 3.4 d, the resonance difference ($\Delta\omega_r$) can be used to determine the coupling coefficient ($\kappa \approx \pi\Delta\omega_r(\beta^{(1)} + \beta^{(2)})/2$).

Another interesting case is presented in figure 3.4e-f, where the coupling between bus waveguide and mode 2 has been turned off ($\theta_2 = 0$). In this case, the resonances of mode 2 only appear when coupled with the resonances of mode 1. An intuitive explanation is that with $\theta_2 = 0$, mode 2 is reliant on mode 1 to supply power. Therefore, in the places that mode 1 is not resonant, no power can be coupled to mode 2. The FSR of mode 2 can be determined from this profile, but the absence of resonances beyond the mode-crossing makes the GVD and intrinsic losses hard to determine.

3.3 Linearly coupled microrings

The coupled transverse modes, discussed in the previous section, exhibit a modified dispersion near the mode crossing which can be used for generating dark DKS. However, their main drawback is that the coupling coefficient is hard to control in fabrication since it is enabled by parasitic effects such as sidewall roughness. Furthermore, the resonance locations of the two transverse modes cannot be tuned separately, due to the fact that the two modes occupy the same physical space. Controlling these two aspects is critical for achieving dark DKS reliably.

An alternative approach is to move transverse mode 2 into a second cavity placed in close proximity to the first cavity such that they become linearly coupled, i.e. using a single transverse mode in each ring. Thus the coupling coefficient between modes can be easily controlled in design by controlling the distance between rings.

Another key benefit of the two ring approach is that the resonance locations of the two modes can be tuned separately [68], tuning the location of the avoided mode crossing. Such tuning can be achieved by heating one of the rings, which causes an increase in the refractive index, shifting the resonances [69, 70]. This was demonstrated in Paper C, enabling dark DKS generation in multiple resonances.

The coupling regimes of the two coupled rings can be approximated with matrices:

$$\begin{bmatrix} E_{out} \\ E_2 \end{bmatrix} = \begin{bmatrix} r_1 & it_1 \\ it_1 & r_1 \end{bmatrix} \begin{bmatrix} E_{in} \\ E_1 \end{bmatrix}, \tag{3.13}$$

$$\begin{bmatrix} E_6 \\ E_4 \end{bmatrix} = \begin{bmatrix} r_2 & it_2 \\ it_2 & r_2 \end{bmatrix} \begin{bmatrix} E_5 \\ E_3 \end{bmatrix}, \tag{3.14}$$

where the input and output fields are depicted in figure 3.5. Note that one of the main differences from the transverse mode model is that there is no coupling from bus waveguide to mode 2 (i.e. the mode in ring 2). An important consequence is that the resonances of ring 2 will only appear when in the vicinity of ring 1 resonance, as was displayed in figure 3.4e. This mean that the characterization of ring 2 will essentially be limited to only the FSR.

It should be noted that the transverse modes of the rings are in practice made identical, achieving a difference of $2 - 5\%$ in FSR by designing the rings with different lengths. However, when modeling these rings in this thesis, the FSR difference will be achieved by changing the

group index, assuming ring 2 has the same length as ring 1. This is a rather crude approximation, but sufficiently accurate considering the limitations to the characterization of ring 2.

The propagation in the microrings is derived in a manner similar to equation 3.3.

$$\frac{\partial E_n}{\partial z} = -\frac{\alpha_n}{2}E_n + i\beta^{(n)}(\Delta\omega)E_n, \tag{3.15}$$

where n stands for the mode in ring n. Using a procedure similar to [71], the transmission can be derived as

$$T = \frac{E_{out}}{E_{in}} = \frac{r_1 - Ka_1e^{i\beta^{(1)}L}}{1 - Kr_1a_1e^{i\beta^{(1)}L}}, \tag{3.16}$$

$$K = \frac{r_2 - a_2e^{i\beta^{(2)}L}}{1 - r_2a_2e^{i\beta^{(2)}L}}, \tag{3.17}$$

where $a_n = e^{-\alpha_n L/2}$. This model was used with the same parameters as presented in figure 3.4e, with the same overall coupling between modes per roundtrip ($t_2 = \kappa L = 0.075$). The resulting transmission spectrum is virtually identical to figure 3.4e. This can be understood by applying the mean-field approximation, which is valid when the intracavity fields do not change significantly over a roundtrip. This assumes that coupling rate between modes can be evenly distributed over a roundtrip, but this modifies equation 3.15 into

$$\begin{aligned}\frac{\partial E_1}{\partial z} &= -\frac{\alpha_1}{2}E_1 + i\beta^{(1)}(\Delta\omega)E_1 + i\kappa' E_2,\\ \frac{\partial E_2}{\partial z} &= -\frac{\alpha_2}{2}E_2 + i\beta^{(2)}(\Delta\omega)E_2 + i\kappa' E_1,\end{aligned} \tag{3.18}$$

where $\kappa' = \frac{t_2}{L}$. Thus, this equation becomes identical to the equation 3.11. The two coupled rings can therefore be accurately modelled and characterized using same methods as described for the coupled transverse modes.

Chapter 4

Soliton generation in microresonators

A nonlinear microresonator cavity has the ability to maintain a dissipative Kerr soliton (DKS). The process relies on the parametric conversion of a CW-pump field to neighboring frequency components. This chapter serves as a brief introduction to DKS's and the nonlinear effects in microresonators. The first section covers nonlinear dynamics in a single cavity. The second section covers DKS generation in anomalous dispersion microresonators. The third section discusses DKS generation in normal dispersive waveguides, both considering single-mode operation and linearly-coupled modes.

4.1 Nonlinear dynamics in a single cavity

The modeling of the nonlinear operation in a single-mode microresonator can be described in two parts: A nonlinear propagation over a full roundtrip and a coupling regime exchanging optical power between bus waveguide and ring. This system of equations is known for forming the Ikeda map [72]. These equations include a modified NLSE and the coupling matrix from equation 3.1

$$\begin{bmatrix} A_{out} \\ A_2 \end{bmatrix} = \begin{bmatrix} r & it \\ it & r \end{bmatrix} \begin{bmatrix} A_{in} \\ A_1 \end{bmatrix}, \tag{4.1}$$

$$\frac{\partial A}{\partial z} = i\gamma|A|^2 A - \frac{\alpha}{2}A + i\beta_0 A - \frac{i\beta_2}{2}\frac{\partial^2 A}{\partial t^2} + \frac{i\beta_3}{6}\frac{\partial^3 A}{\partial t^3}. \tag{4.2}$$

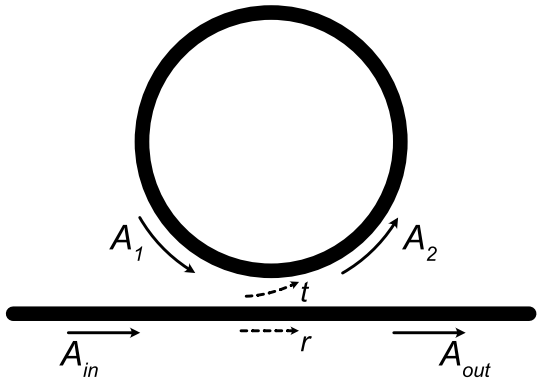

Figure 4.1: A basic layout of the microring resonator: a bus waveguide coupled to a ring waveguide.

Note that the term, β_0, signifies the phase shift per unit length of the input field (A_{in}) compared to the resonance of the cavity. It is often expressed in terms of the detuning $\delta_0 = -\beta_0 L$, which accounts for the accumulated phase shift of the pump compared to nearest resonance. The coupling between bus waveguide and ring is often presented in terms of power as $\theta = t^2$.

Defining the internal field (A) in a time window, spanning the duration of a cavity roundtrip, a full roundtrip of the intracavity field can be easily simulated. This is done by first applying the coupling equation and then simulating propagation through the full length of the ring by solving equation 4.2 with the split-step method. Realistically, such a field will include noise due to the quantized nature of light, which is included in the simulation by adding a photon with a random phase into each spectral bin onto the laser [73, 74].

4.1.1 The Lugiato-Lefever equation

The Ikeda map can be approximated as a single equation, which is sometimes called the Lugiato-Lefever equation (LLE). It is named after the authors who first derived it to describe the optical spatial field in a nonlinear cavity [75], but it was later shown that it also applies for temporal fields [76].

To derive the LLE the intracavity field is assumed not to change significantly over the span of a single roundtrip. As such, the nonlinear

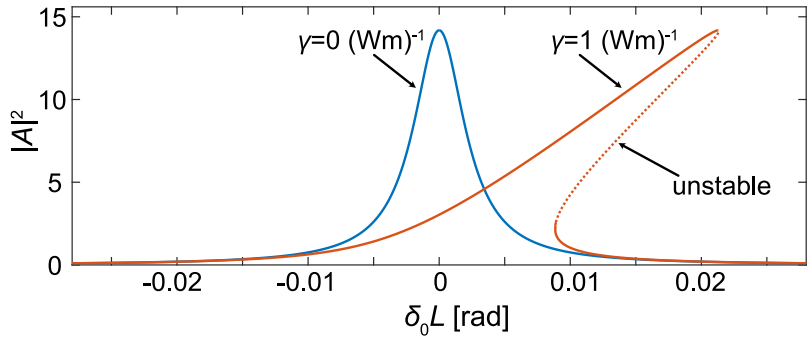

Figure 4.2: Solutions for the intracavity power assuming CW steady-state, with blue and red show the contrast between linear and nonlinear regime. The parameters were set as $P_{in} = 20\,mW$, $\sigma = 0.0024$ and $L = 1.5\,mm$.

propagation through the length of the cavity (L) can be approximated by

$$A_1^{(n)} = A_2^{(n-1)} + L\frac{\partial A_1^{(n)}}{\partial z}, \tag{4.3}$$

where n presents the number of roundtrips. The coupling regime gives

$$A_2^{(n-1)} = A_1^{(n-1)}(1-\theta) + \sqrt{\theta}A_{in}, \tag{4.4}$$

where, assuming that the coupling rate is low, the approximation $\sqrt{1-\theta} \approx 1 - \theta/2$ has been applied. Combining equations 4.3 and 4.4, and substituting 4.2 leads to the LLE equation:

$$\frac{\partial A}{\partial \tau} = \frac{A_1^{(n)} - A_1^{(n-1)}}{t_R} = \frac{1}{t_R}(-\sigma - i\delta_0 - L\frac{i\beta_2}{2}\frac{\partial^2}{\partial t^2} + L\frac{i\beta_3}{6}\frac{\partial^3}{\partial t^3} + iL\gamma|A|^2)A + i\sqrt{\theta}A_{in}, \tag{4.5}$$

where $\sigma = \frac{\theta+\alpha L}{2}$ and t_R is the roundtrip time, and τ is the slow time. This equation has been widely used to investigate the dynamics of nonlinear cavities, such as bistability [76, 77], existence regimes of waveforms [77–79], modulational instability [73, 80] and impact of parameters on spectral features [37, 81].

4.1.2 Bistability

The LLE can be used to describe a CW intracavity field of the cavity in presence of the nonlinear phase shift [76]. Assuming steady-state, the

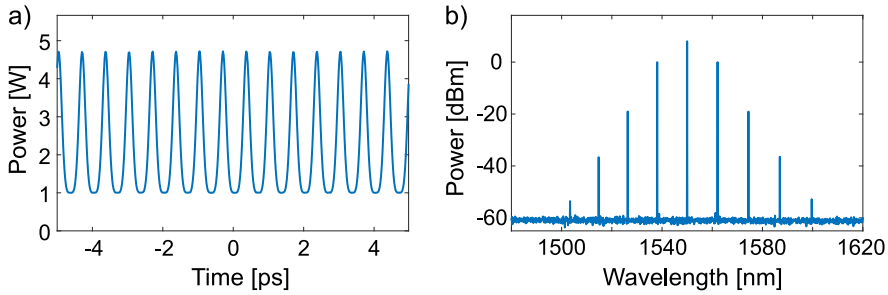

Figure 4.3: a) shows the temporal features of Turing rolls, with b) showing the corresponding spectrum. Parameters were set as $\theta = 0.005$, $\beta_2 = -100 ps^2/km$, $L = 1.5\,mm$, $FSR = 100\,GHz$, $\alpha = 0.5\,m^{-1}$, $\gamma = 1\,(Wm)^{-1}$, $\delta_0 = 0$, $P_{in} = 10\,mW$.

LLE is reduced to

$$i\sqrt{\theta}A_{in} = (-\sigma - i\delta_0 + i\gamma L|A|^2)A. \tag{4.6}$$

Multiplying each side of the equation with its conjugate results in [81]

$$\theta|A_{in}|^2 = (\sigma^2 + \delta_0^2 + \gamma^2 L^2 P^2 - 2\delta_0\gamma LP)P, \tag{4.7}$$

where $P = |A|^2$ is the intracavity power, which can be easily solved numerically. Then, by taking the angle of 4.6, the angle of the intracavity field is found as

$$\angle A = \angle(iA_{in}) - \angle(-\sigma - i\delta_0 + i\gamma L|A|^2). \tag{4.8}$$

Using these equations, the power build-up in a resonant cavity is plotted in figure 4.2. It shows how the resonances of the cavity become 'tilted' in the presence of a nonlinear phase shift. This leads to three possible solutions for the intracavity field, one of which is unstable. The area of bistability has been closely linked with the appearance of DKS's [78,81]. A part of the reason is that the higher branch of the bistability has high power, enhancing the nonlinearities that generate and maintain the DKS. As will be discussed in section 4.3, another intuitive reason is that the DKS form as a transition between the bistable levels.

4.1.3 Modulational instability

The bistability analysis above only considered CW solutions. However, in the presence of small perturbations (e.g. noise), the microcavity can exhibit modulational instability (MI). This occurs when the CW field (P) provides parametric amplification to other frequency components which outweighs the cavity losses. This can lead to an oscillating temporal field [82], commonly named Turing rolls [78, 83], which are displayed in figure 4.3. In anomalous GVD microrings, by tuning the power or frequency of the CW laser, the Turing rolls can change shape and turn into bright DKS [84]. This is enabled by the fact that the existence regimes of Turing rolls and bright DKS are linked, either directly or through an intermediate chaotic regime [78, 85]. The presence of MI near the existence regime of DKS is thus essential for initiation from a CW laser.

DKS initiation in the normal GVD regime also requires Turing rolls. However, due to the lack of phase matching in single-mode waveguides, MI will be extremely hard to achieve. The phase-matching condition for MI, assuming negligible higher-order dispersion, can be derived from the LLE as [73]

$$\beta_2 = 2\frac{\delta_0 - 2\gamma LP}{\Delta\omega^2 L}, \tag{4.9}$$

where $\Delta\omega$ signifies the frequency where phase matching occurs (i.e. maximum parametric amplification). Note that the $(\delta_0 - 2\gamma LP)$ sets a limitation to the sign of the GVD. MI is accessible in the anomalous GVD regime when $(\delta_0 < 2\gamma LP)$, which only requires $\delta_0 = 0$ to be fulfilled. However, in the normal dispersion regime, the requirement is $(\delta_0 > 2\gamma LP)$, where Turing rolls can only be found using excessive pump power and high detuning [78]. Furthermore, the existence regime of dark DKS and Turing rolls are not linked, since dark DKS exist in the regime where $(\delta_0 < 2\gamma LP)$. Dark DKS are thus virtually impossible to achieve in single-mode normal GVD microrings.

One way of achieving phase matching in normal GVD waveguides is by modifying the dispersion profile via coupling to another mode [27, 32, 33, 86, 87]. As discussed in section 3.2, linearly coupled transverse modes or linearly coupled microcavities can effectively introduce localized anomalous GVD in normal GVD waveguides. This was a key factor in Paper B and Paper C, where such mode-coupling eased the phase-matching condition, allowing a DKS to be generated from Turing

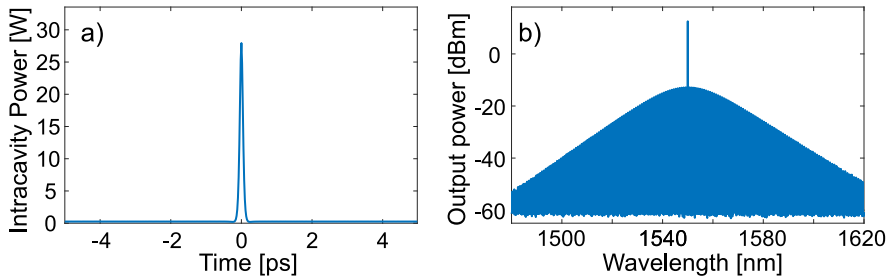

Figure 4.4: a) shows the temporal features of a bright DKS, with b) showing the corresponding spectrum. Parameters were set as $\theta = 0.005$, $\beta_2 = -100ps^2/km$, $L = 1.5mm$, $FSR = 100GHz$, $\alpha = 0.5m^{-1}$, $\gamma = 1(Wm)^{-1}$, $\delta_0 = 0.02$, $P_{in} = 20\,mW$. The soliton was initiated using the theoretically derived envelope of the bright DKS.

rolls.

Phase matching is not the only condition for MI. A second condition requires the intracavity power to rise beyond the gain threshold of the parametric oscillations [82, 88]. This sets a threshold input power, described by [73]

$$P_{in,th} = \frac{1}{\gamma L}\left(2\sigma^2 + (\delta_0 - \sigma)^2\right), \tag{4.10}$$

where $\sigma = \frac{\theta+\alpha L}{2} \approx \frac{\omega_0 n_g L}{\pi c_0 Q}$. This sets a $1/Q^2$ condition for the input power to achieve MI, underlining once again the importance of minimizing the losses of the cavity to realize low power operation. Thus, demonstrations of low-power operation of microcombs depend on realizing microcavities with high quality-factors [35, 36]. Indeed, high quality-factors were one of the key factors in Paper C to realize microcomb generated from only 2.5 mW of laser power.

4.2 Generation of DKS in anomalous dispersion microresonators

The bright DKS was theoretically described in optical cavities as early as the 90's [77, 89]. It is essentially a soliton-like pulse which sits on top of a CW background defined by the lower level of the CW bistability (see figure 4.4). The spectrum has a smooth envelope, with a line separation

equal to the rate at which the DKS circulates the cavity. Both the temporal and spectral amplitudes of the bright DKS can be derived as a hyperbolic secant from the LLE [25, 37, 81]. Such studies have shown that the conversion efficiency (the output power of generated comb lines divided by the input power) is fundamentally limited, which can lead to a lack of power in the generated comb lines. This became the inspiration for the numerical analysis of conducted in Paper A, where the conversion efficiency and line power of bright DKS is compared to the dark DKS.

Bright DKS were first experimentally demonstrated in a nonlinear fiber cavity in 2010 [53] and would appear in microresonators a few years later [25]. These waveforms can be initiated using a CW laser at a constant pump power, tuning the laser frequency into resonance from the blue side towards the red. Figure 4.5a shows the simulated evolution of the intracavity power as the laser detuning is changed linearly with time. The cavity goes through a state of MI, where Turing rolls are generated, into a chaotic state. At a certain detuning, the chaos subsides, with multiple bright DKS's appearing as shown in figure 4.5b. It shows that multiple bright DKS, all having the same shape, can coexist in the cavity. The spectrum (figure 4.5b) of these multisoliton states is relatively uneven and therefore often undesirable. Due to the chaotic regime, the number of generated DKS is generally not deterministic. However, this can be overcome by involving methods where the laser frequency is slowly shifted towards the blue side or via careful tuning of the microring temperature [31, 90].

Since its first demonstration, the bright DKS has been heavily researched [21]. Multiple demonstrations have been conducted, such as microwave generation [91], ultrafast ranging and detection [92], spectrogram calibration for exoplanet detection [93] and optical atomic clocks [94].

Anomalous GVD microrings can also exhibit waveforms beyond the bright DKS. The Soliton crystal is one example, which can be viewed as the arrangement of multisoliton states into fixed patterns [26]. Another example is the dispersive wave (Cherenkov radiation), which manifests itself when the part of the spectrum has normal GVD due to third-order dispersion. This leads the DKS developing oscillatory tails [95]. Recent efforts have moved towards generating DKS in coupled anomalous microresonators. The super-efficient soliton has been theoretically predicted in such coupled microrings [96], promising a conversion efficiency $> 90\%$, far exceeding that of the regular bright DKS. It is generated in an

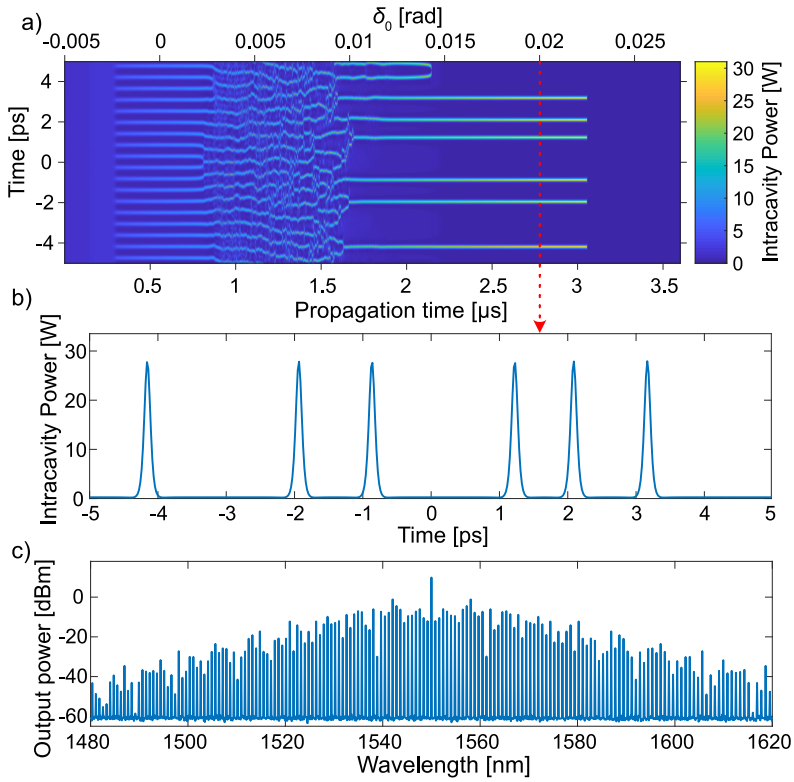

Figure 4.5: a) shows the evolution of the temporal field in an anomalous microring as the detuning is changed linearly with propagation time. It shows the generation of Turing patterns at $\delta_0 = 0$, chaos at $\delta_0 = 0.005 rad$ and solitons appearing after $\delta_0 = 0.01\ rad$. b) shows the temporal field at $\delta_0 = 0.02\ rad$, with c) showing the corresponding spectrum. Parameters used were $\theta = 0.005$, $\beta_2 = -100 ps^2/km$, $L = 1.5mm$, $FSR = 100GHz$, $\alpha = 0.5m^{-1}$, $\gamma = 1(Wm)^{-1}$, $P_{in} = 20\ mW$.

anomalous GVD microresonator which is coupled to a normal dispersion microring. The input pump is first coupled from a bus waveguide to the normal GVD ring, where power builds up. The enhanced power in the normal GVD ring is then used to feed the anomalous GVD ring where the soliton is generated. While this is a promising design for energy-efficient microcombs, it has yet to be demonstrated.

4.3 Generation of DKS in normal dispersion microresonators

A DKS can be maintained in normal GVD single-mode microresonators. It is essentially a dark pulse in a CW background with oscillations in the bottom that decay towards the middle (see figure 4.6) [27]. The CW background and the bottom ripples are closely related to the CW steady-steady state solution of the bistability, where the dark DKS appears to switch between these two states. As such, it has been described as two switching waves, which move towards each other until their oscillatory tails lock together [97, 98]. A peculiar result of this is that the resulting pulse can exist in different states depending on how these oscillatory tails lock together, with each state having varying widths and a different number of ripples at the bottom of the pulse [79]. Switching between these states was observed in Paper B as a change in the number of oscillations in the comb spectrum.

The spectrum of a dark DKS is distinctly different from the bright DKS. It displays a number of ripples that are somewhat linked to the number of ripples in the temporal field. Thus, the spectrum is much less even compared to the bright DKS. However, the conversion efficiency of these waveforms is usually higher than 20% [38], much higher than their bright counterpart in anomalous GVD. This results in higher line power, as was discussed in Paper A, making them attractive for optical telecommunication experiments. Indeed, dark DKS's were employed in such experiments in Papers D and H.

It has to be noted that while the discussion has so far focused on dark DKS in single-mode microresonators. However, such operation has not been demonstrated in practice. The problem lies in that the dark DKS cannot be initiated from a CW laser in a normal GVD microring due to a lack of MI, as was discussed in section 4.1.3. Demonstrated dark DKS have thus required perturbed GVD profile to achieve the phase matching required for MI, i.e. by employing an avoided mode-crossing as discussed in section 3.2 and 3.3,

The first experimental demonstrations of dark DKS were generated by pumping a resonance in a mode-crossing enabled by two transverse modes [27,87,99]. These have been useful in demonstrating the dynamics of dark DKS, such as in Paper B, where it was shown that dark DKS are generated deterministically by simply tuning a CW laser into resonance from the blue side.

However, as discussed in section 3.3, the coupled transverse modes offer limited control over the linear mode-coupling strength and location of the avoided mode-crossing. If either of these factors is not set correctly, a DKS might not be attainable. Furthermore, if the avoided mode-crossing is not tunable, a DKS is generally only achieved in one resonance. This difficulty is perhaps the reason why dark DKS have not been used as commonly in demonstrations compared to the bright DKS.

More recent efforts of dark DKS generation have featured linearly coupled microresonators, where the avoided mode-crossing can be moved separately via microheaters on each microring [68]. Microcombs from such a design were first demonstrated in [27], with [33] showing later improvements. Paper C demonstrated unequivocally a DKS in linearly coupled microresonators.

DKS's generated in an avoided mode-crossing can also exhibit a significant change in shape compared to the single-mode dark DKS. Pumped at near the center of a mode-crossing, they are typically asymmetrical due to the asymmetric perturbation of the crossing [100]. They can also exhibit a spectrum with no ripples, but a flat-top [32]. Such waveforms have been found in simulations when the pump resonance is shifted compared to other resonances, and are sometimes called platicons [101].

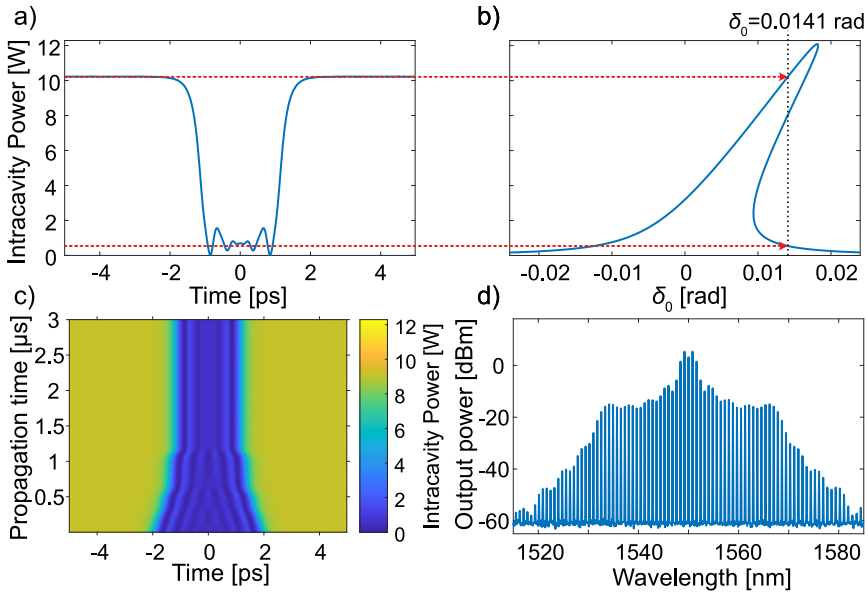

Figure 4.6: a) shows the temporal characteristics of a dark DKS circulating in a single-mode normal dispersion cavity. b) shows the bistability for the same cavity, with a vertical dashed line indicating the detuning at which the dark DKS operates. The red lines drawn between a) and b) show that the upper and lower power levels of the dark pulse strongly linked to the upper and lower branch of the bistability, where the dark DKS can be considered to switch bete. c) shows how the dark DKS is formed from an initial condition of a dark square pulse with amplitudes and phase corresponding to the CW bistability solutions. d) shows the spectrum that corresponds to the dark DKS. Parameters were set as $\theta = 0.005$, $\beta_2 = 100\, ps^2/km$, $L = 1.5\, mm$, $FSR = 100\, GHz$, $\alpha = 0.5\, m^{-1}$, $\gamma = 1\, (Wm)^{-1}$, $\delta_0 = 0.0141$, $P_{in} = 20\, mW$.

Chapter 5

Future outlook

In this thesis, I have studied the dynamics of dark DKS both experimentally and in simulations. Here are a few things I consider interesting for future work

- My studies in Paper C considered dark DKS generation enabled by linearly coupled microrings. The dynamics of this system is considerably more complicated than the single-mode system. Further exploration into the dynamics of coupled rings could lead to the discovery of new dynamics, exotic waveforms and new opportunities in the field of microcomb.
- Improving the conversion efficiency and spectral shape of microcombs would be of high value for several applications. Superefficient solitons have been suggested, but not realized in microcavities. Realizing such a waveform would be a breakthrough in the field of microcombs. Another thing worth investigating is the generation of a superefficient dark DKS in a normal dispersion cavity.
- The linearly coupled microring in Paper C demonstrated impressive performance. The next step with those rings would be to use them in demonstrations within applications such as telecommunications or dual-comb spectroscopy.

Chapter 6

Summary of Papers

Paper A

Superchannel engineering of microcombs for optical communications,
Journal of the Optical Society of America B, 36, 8, 2013-2022, 2019.

Here, we conduct a numerical investigation into the performance of both dark and bright DKS for generating frequency carriers for fiber optical communications. We discuss the benefits of using multiple narrow microcomb sources, each constituting a superchannel, compared to using a broad microcomb source. We discover that the line power of bright and dark DKS follow the same scaling in terms of input power and number of lines generated, showing that dark DKS can offer up to 3 dB higher line power compared to the bright DKS.

My contributions: I conducted the simulations, I wrote the paper with support from co-authors, I presented the work at CLEO 2018

Paper B

Switching dynamics of dark-pulse Kerr comb states in optical microresonators,
arXiv:1910.11035, 2019

In this work, we investigate the dynamics of dark DKS comb generation, both experimentally and numerically. Spectrally probing

the pump resonance as the dark DKS is generated, we discover that an extra resonance appears once the comb is initiated. We find that the two resonances are closely linked to the bistability of the cavity. We also find that the dark DKS spectra exhibits switching between different states. Numerical simulations accurately replicated the comb spectra, showing that the different states correspond to dark pulses with different number of oscillations.

My contributions: I conducted single-mode simulations to verify the VNA scans, I assisted with lab measurements, I presented the part of the work that featured hot cavity spectroscopy at CLEO EU 2019.

Paper C

Dissipative Kerr solitons in photonic molecules,
arXiv:2007.02608, 2020.

Here, we demonstrate DKS generated from linearly-coupled normal dispersion microrings. Using a microheater on one of the rings to control the coupling interaction, we demonstrate that these structures can generate DKS with high conversion efficiency at low input power in a reproducible manner. We show through numerical simulations that the dynamics of these DKS are enabled by the linear coupling of two cavities. We numerically demonstrate that this design offers DKS's with a larger existence regime compared to dark DKS in single-mode cavities.

My contributions: I conducted the lab experiments, I replicated the microcombs numerically, I assisted with numerical characterization, I wrote parts of the paper, I presented the work at CLEO 2020.

References

[1] J. L. Hall, "Nobel Lecture: Defining and measuring optical frequencies," *Reviews of Modern Physics*, vol. 78, no. 4, pp. 1279–1295, 2006.

[2] T. W. Hänsch, "Nobel Lecture: Passion for precision," *Reviews of Modern Physics*, vol. 78, no. 4, pp. 1297–1309, 2006.

[3] S. A. Diddams, D. J. Jones, J. Ye, S. T. Cundiff, J. L. Hall, J. K. Ranka, R. S. Windeler, R. Holzwarth, T. Udem, and T. W. Hänsch, "Direct Link between Microwave and Optical Frequencies with a 300 THz Femtosecond Laser Comb," *Physical Review Letters*, vol. 84, no. 22, pp. 5102–5105, 2000.

[4] R. Holzwarth, T. Udem, T. W. Hänsch, J. C. Knight, W. J. Wadsworth, and P. S. J. Russell, "Optical Frequency Synthesizer for Precision Spectroscopy," *Physical Review Letters*, vol. 85, no. 11, pp. 2264–2267, 2000.

[5] S. T. Cundiff and J. Ye, "Colloquium : Femtosecond optical frequency combs," *Reviews of Modern Physics*, vol. 75, no. 1, pp. 325–342, 2003.

[6] S. A. Diddams, K. Vahala, and T. Udem, "Optical frequency combs: Coherently uniting the electromagnetic spectrum," *Science*, vol. 369, no. 6501, p. eaay3676, 2020.

[7] S. M. Brewer, J.-S. Chen, A. M. Hankin, E. R. Clements, C. W. Chou, D. J. Wineland, D. B. Hume, and D. R. Leibrandt, "An $^{27}Al^{+}$ quantum-logic clock with systematic uncertainty below 10^{-18}," *Physical Review Letters*, vol. 123, no. 3, p. 033201, 2019.

[8] R. A. McCracken, J. M. Charsley, and D. T. Reid, "A decade of astrocombs: recent advances in frequency combs for astronomy," *Optics Express*, vol. 25, no. 13, p. 15058, 2017.

[9] I. Coddington, N. Newbury, and W. Swann, "Dual-comb spectroscopy," *Optica*, vol. 3, no. 4, pp. 414–426, 2016.

[10] X. Xie, R. Bouchand, D. Nicolodi, M. Giunta, W. Hänsel, M. Lezius, A. Joshi, S. Datta, C. Alexandre, M. Lours, P.-A. Tremblin, G. Santarelli, R. Holzwarth, and Y. Le Coq, "Photonic microwave signals with zeptosecond-level absolute timing noise," *Nature Photonics*, vol. 11, no. 1, pp. 44–47, 2017.

[11] L. Lundberg, M. Karlsson, A. Lorences-Riesgo, M. Mazur, V. Torres-Company, J. Schröder, and P. Andrekson, "Frequency Comb-Based WDM Transmission Systems Enabling Joint Signal Processing," *Applied Sciences*, vol. 8, no. 5, p. 718, 2018.

[12] V. Torres-Company, J. Schröder, A. Fülöp, M. Mazur, L. Lundberg, Ó. B. Helgason, M. Karlsson, and P. A. Andrekson, "Laser Frequency Combs for Coherent Optical Communications," *Journal of Lightwave Technology*, vol. 37, no. 7, pp. 1663–1670, 2019.

[13] H. Haus, "Mode-locking of lasers," *IEEE Journal of Selected Topics in Quantum Electronics*, vol. 6, no. 6, pp. 1173–1185, 2000.

[14] L. E. Hargrove, R. L. Fork, and M. A. Pollack, "Locking of He–Ne laser modes induced by synchronous intracavity modulation," *Applied Physics Letters*, vol. 5, no. 1, pp. 4–5, 1964.

[15] V. Torres-Company and A. M. Weiner, "Optical frequency comb technology for ultra-broadband radio-frequency photonics," *Laser & Photonics Reviews*, vol. 8, no. 3, pp. 368–393, 2014.

[16] K. Beha, D. C. Cole, P. Del'Haye, A. Coillet, S. A. Diddams, and S. B. Papp, "Electronic synthesis of light," *Optica*, vol. 4, no. 4, pp. 406–411, 2017.

[17] D. R. Carlson, D. D. Hickstein, W. Zhang, A. J. Metcalf, F. Quinlan, S. A. Diddams, and S. B. Papp, "Ultrafast electro-optic light with subcycle control," *Science*, vol. 361, no. 6409, pp. 1358–1363, 2018.

[18] A. L. Gaeta, M. Lipson, and T. J. Kippenberg, "Photonic-chip-based frequency combs," *Nature Photonics*, vol. 13, no. 3, pp. 158–169, 2019.

[19] S. Liu, X. Wu, D. Jung, J. C. Norman, M. J. Kennedy, H. K. Tsang, A. C. Gossard, and J. E. Bowers, "High-channel-count 20 GHz passively mode-locked quantum dot laser directly grown on Si with 4.1 Tbit/s transmission capacity," *Optica*, vol. 6, no. 2, pp. 128–134, 2019.

[20] M. Zhang, B. Buscaino, C. Wang, A. Shams-Ansari, C. Reimer, R. Zhu, J. M. Kahn, and M. Lončar, "Broadband electro-optic frequency comb generation in a lithium niobate microring resonator," *Nature*, vol. 568, no. 7752, pp. 373–377, 2019.

[21] T. J. Kippenberg, A. L. Gaeta, M. Lipson, and M. L. Gorodetsky, "Dissipative Kerr solitons in optical microresonators," *Science*, vol. 361, no. 6402, p. eaan8083, 2018.

[22] T. J. Kippenberg, R. Holzwarth, and S. A. Diddams, "Microresonator-Based Optical Frequency Combs," *Science*, vol. 332, no. 6029, pp. 555–559, 2011.

[23] P. Del'Haye, A. Schliesser, O. Arcizet, T. Wilken, R. Holzwarth, and T. J. Kippenberg, "Optical frequency comb generation from a monolithic microresonator," *Nature*, vol. 450, no. 7173, pp. 1214–1217, 2007.

[24] A. Pasquazi, M. Peccianti, L. Razzari, D. J. Moss, S. Coen, M. Erkintalo, Y. K. Chembo, T. Hansson, S. Wabnitz, P. Del'Haye, X. Xue, A. M. Weiner, and R. Morandotti, "Micro-combs: A novel generation of optical sources," *Physics Reports*, vol. 729, pp. 1–81, 2018.

[25] T. Herr, V. Brasch, J. D. Jost, C. Y. Wang, N. M. Kondratiev, M. L. Gorodetsky, and T. J. Kippenberg, "Temporal solitons in optical microresonators," *Nature Photonics*, vol. 8, no. 2, pp. 145–152, 2014.

[26] D. C. Cole, E. S. Lamb, P. Del'Haye, S. A. Diddams, and S. B. Papp, "Soliton crystals in Kerr resonators," *Nature Photonics*, vol. 11, no. 10, pp. 671–676, 2017.

[27] X. Xue, Y. Xuan, Y. Liu, P.-H. Wang, S. Chen, J. Wang, D. E. Leaird, M. Qi, and A. M. Weiner, "Mode-locked dark pulse Kerr combs in normal-dispersion microresonators," *Nature Photonics*, vol. 9, no. 9, pp. 594–600, 2015.

[28] P. Del'Haye, A. Coillet, T. Fortier, K. Beha, D. C. Cole, K. Y. Yang, H. Lee, K. J. Vahala, S. B. Papp, and S. A. Diddams, "Phase-coherent microwave-to-optical link with a self-referenced microcomb," *Nature Photonics*, vol. 10, no. 8, pp. 516–520, 2016.

[29] A. Fülöp, M. Mazur, A. Lorences-Riesgo, Ó. B. Helgason, P.-H. Wang, Y. Xuan, D. E. Leaird, M. Qi, P. A. Andrekson, A. M. Weiner, and V. Torres-Company, "High-order coherent communications using mode-locked dark-pulse Kerr combs from microresonators," *Nature Communications*, vol. 9, no. 1, p. 1598, 2018.

[30] M. Mazur, M.-G. Suh, A. Fülöp, J. Schröder, V. Torres-Company, M. Karlsson, K. J. Vahala, and P. A. Andrekson, "Enabling high spectral efficiency coherent superchannel transmission with soliton microcombs," arXiv:1812.11046, 2018.

[31] H. Guo, M. Karpov, E. Lucas, A. Kordts, M. H. P. Pfeiffer, V. Brasch, G. Lihachev, V. E. Lobanov, M. L. Gorodetsky, and T. J. Kippenberg, "Universal dynamics and deterministic switching of dissipative Kerr solitons in optical microresonators," *Nature Physics*, vol. 13, no. 1, pp. 94–102, 2017.

[32] X. Xue, Y. Xuan, P.-H. Wang, Y. Liu, D. E. Leaird, M. Qi, and A. M. Weiner, "Normal-dispersion microcombs enabled by controllable mode interactions," *Laser & Photonics Reviews*, vol. 9, no. 4, pp. L23–L28, 2015.

[33] B. Y. Kim, Y. Okawachi, J. K. Jang, M. Yu, X. Ji, Y. Zhao, C. Joshi, M. Lipson, and A. L. Gaeta, "Turn-key, high-efficiency Kerr comb source," *Optics Letters*, vol. 44, no. 18, pp. 4475–4478, 2019.

[34] L. Chang, W. Xie, H. Shu, Q.-F. Yang, B. Shen, A. Boes, J. D. Peters, W. Jin, C. Xiang, S. Liu, G. Moille, S.-P. Yu, X. Wang, K. Srinivasan, S. B. Papp, K. Vahala, and J. E. Bowers, "Ultra-efficient frequency comb generation in AlGaAs-on-insulator microresonators," *Nature Communications*, vol. 11, no. 1, p. 1331, 2020.

[35] B. Stern, X. Ji, Y. Okawachi, A. L. Gaeta, and M. Lipson, "Battery-operated integrated frequency comb generator," *Nature*, vol. 562, no. 7727, pp. 401–405, 2018.

[36] B. Shen, L. Chang, J. Liu, H. Wang, Q.-F. Yang, C. Xiang, R. N. Wang, J. He, T. Liu, W. Xie, J. Guo, D. Kinghorn, L. Wu, Q.-X. Ji, T. J. Kippenberg, K. Vahala, and J. E. Bowers, "Integrated turnkey soliton microcombs," *Nature*, vol. 582, no. 7812, pp. 365–369, 2020.

[37] C. Bao, L. Zhang, A. Matsko, Y. Yan, Z. Zhao, G. Xie, A. M. Agarwal, L. C. Kimerling, J. Michel, L. Maleki, and A. E. Willner, "Nonlinear conversion efficiency in Kerr frequency comb generation," *Optics Letters*, vol. 39, no. 21, pp. 6126–6129, 2014.

[38] X. Xue, P.-H. Wang, Y. Xuan, M. Qi, and A. M. Weiner, "Microresonator Kerr frequency combs with high conversion efficiency," *Laser & Photonics Reviews*, vol. 11, no. 1, p. 1600276, 2017.

[39] A. Hasegawa, "An historical review of application of optical solitons for high speed communications," *Chaos: An Interdisciplinary Journal of Nonlinear Science*, vol. 10, no. 3, pp. 475–485, 2000.

[40] G. P. Agrawal, *Nonlinear Fiber Optics*, 5th ed. Elsevier, 2012.

[41] J. Hult, "A Fourth-Order Runge–Kutta in the Interaction Picture Method for Simulating Supercontinuum Generation in Optical Fibers," *Journal of Lightwave Technology*, vol. 25, no. 12, pp. 3770–3775, 2007.

[42] J. S. Russell, "Report of the fourteenth meeting of the British Association for the Advancement of Science," York, 1844 (London 1845), pp. 311–390.

[43] N. J. Zabusky and M. D. Kruskal, "Interaction of "Solitons" in a Collisionless Plasma and the Recurrence of Initial States," *Physical Review Letters*, vol. 15, no. 6, pp. 240–243, 1965.

[44] A. Hasegawa and F. Tappert, "Transmission of stationary nonlinear optical pulses in dispersive dielectric fibers. I. Anomalous dispersion," *Applied Physics Letters*, vol. 23, no. 3, pp. 142–144, 1973.

[45] K. Blow and N. Doran, "The asymptotic dispersion of soliton pulses in lossy fibres," *Optics Communications*, vol. 52, no. 5, pp. 367–370, 1985.

[46] N. Akhmediev and A. Ankiewicz, *Dissipative Solitons: From Optics to Biology and Medicine*, ser. Lecture Notes in Physics. Berlin, Heidelberg: Springer Berlin Heidelberg, 2008, vol. 751.

[47] P. Grelu and N. Akhmediev, "Dissipative solitons for mode-locked lasers," *Nature Photonics*, vol. 6, no. 2, pp. 84–92, 2012.

[48] T. Sylvestre, S. Coen, P. Emplit, and M. Haelterman, "Self-induced modulational instability laser revisited: normal dispersion and dark-pulse train generation," *Optics Letters*, vol. 27, no. 7, pp. 482–484, 2002.

[49] L. F. Mollenauer and R. H. Stolen, "The soliton laser," *Optics Letters*, vol. 9, no. 1, pp. 13–15, 1984.

[50] L. Zhao, D. Tang, T. Cheng, and C. Lu, "Nanosecond square pulse generation in fiber lasers with normal dispersion," *Optics Communications*, vol. 272, no. 2, pp. 431–434, 2007.

[51] W. H. Renninger, A. Chong, and F. W. Wise, "Pulse Shaping and Evolution in Normal-Dispersion Mode-Locked Fiber Lasers," *IEEE Journal of Selected Topics in Quantum Electronics*, vol. 18, no. 1, pp. 389–398, 2012.

[52] J. M. Soto-Crespo, P. Grelu, N. Akhmediev, and N. Devine, "Soliton complexes in dissipative systems: Vibrating, shaking, and mixed soliton pairs," *Physical Review E*, vol. 75, no. 1, p. 016613, 2007.

[53] F. Leo, S. Coen, P. Kockaert, S.-P. Gorza, P. Emplit, and M. Haelterman, "Temporal cavity solitons in one-dimensional Kerr media as bits in an all-optical buffer," *Nature Photonics*, vol. 4, no. 7, pp. 471–476, 2010.

[54] K. J. Vahala, "Optical microcavities," *Nature*, vol. 424, no. 6950, pp. 839–846, 2003.

[55] I. Chremmos, O. Schwelb, and N. Uzunoglu, Eds., *Photonic Microresonator Research and Applications*, ser. Springer Series in Optical Sciences. Boston, MA: Springer US, 2010, vol. 156.

[56] H. Haus and W. Huang, "Coupled-mode theory," *Proceedings of the IEEE*, vol. 79, no. 10, pp. 1505–1518, 1991.

[57] A. Yariv, "Universal relations for coupling of optical power between microresonators and dielectric waveguides," *Electronics Letters*, vol. 36, no. 4, pp. 321–322, 2000.

[58] W. Bogaerts, P. De Heyn, T. Van Vaerenbergh, K. De Vos, S. Kumar Selvaraja, T. Claes, P. Dumon, P. Bienstman, D. Van Thourhout, and R. Baets, "Silicon microring resonators," *Laser & Photonics Reviews*, vol. 6, no. 1, pp. 47–73, 2012.

[59] J. E. Heebner and R. W. Boyd, "Enhanced all-optical switching by use of a nonlinear fiber ring resonator," *Optics Letters*, vol. 24, no. 12, pp. 847–849, 1999.

[60] M. H. P. Pfeiffer, J. Liu, A. S. Raja, T. Morais, B. Ghadiani, and T. J. Kippenberg, "Ultra-smooth silicon nitride waveguides based on the Damascene reflow process: fabrication and loss origins," *Optica*, vol. 5, no. 7, pp. 884–892, 2018.

[61] Z. Ye, K. Twayana, P. A. Andrekson, and V. Torres-Company, "High-Q Si 3 N 4 microresonators based on a subtractive processing for Kerr nonlinear optics," *Optics Express*, vol. 27, no. 24, p. 35719, 2019.

[62] T. Klaassen, J. de Jong, M. van Exter, and J. P. Woerdman, "Transverse mode coupling in an optical resonator," *Optics Letters*, vol. 30, no. 15, pp. 1959–1961, 2005.

[63] J. Zhu, S. K. Özdemir, L. He, and L. Yang, "Controlled manipulation of mode splitting in an optical microcavity by two Rayleigh scatterers," *Optics Express*, vol. 18, no. 23, pp. 23 535–23 543, 2010.

[64] S.-W. Huang, H. Liu, J. Yang, M. Yu, D.-L. Kwong, and C. W. Wong, "Smooth and flat phase-locked Kerr frequency comb generation by higher order mode suppression," *Scientific Reports*, vol. 6, no. 1, p. 26255, 2016.

[65] T. Herr, V. Brasch, J. D. Jost, I. Mirgorodskiy, G. Lihachev, M. L. Gorodetsky, and T. J. Kippenberg, "Mode Spectrum and Temporal Soliton Formation in Optical Microresonators," *Physical Review Letters*, vol. 113, no. 12, p. 123901, 2014.

[66] W.-P. Huang, "Coupled-mode theory for optical waveguides: an overview," *Journal of the Optical Society of America A*, vol. 11, no. 3, pp. 963–983, 1994.

[67] C. Xia, N. Bai, I. Ozdur, X. Zhou, and G. Li, "Supermodes for optical transmission," *Optics Express*, vol. 19, no. 17, p. 16653, 2011.

[68] S. A. Miller, Y. Okawachi, S. Ramelow, K. Luke, A. Dutt, A. Farsi, A. L. Gaeta, and M. Lipson, "Tunable frequency combs based on dual microring resonators," *Optics Express*, vol. 23, no. 16, pp. 21 527–21 540, 2015.

[69] K. Ikeda, R. E. Saperstein, N. Alic, and Y. Fainman, "Thermal and Kerr nonlinear properties of plasma-deposited silicon nitride/ silicon dioxide waveguides," *Optics Express*, vol. 16, no. 17, pp. 12 987–12 994, 2008.

[70] X. Jiang and L. Yang, "Optothermal dynamics in whispering-gallery microresonators," *Light: Science & Applications*, vol. 9, no. 1, p. 24, 2020.

[71] K. Oda, N. Takato, and H. Toba, "A wide-FSR waveguide double-ring resonator for optical FDM transmission systems," *Journal of Lightwave Technology*, vol. 9, no. 6, pp. 728–736, 1991.

[72] K. Ikeda, "Multiple-valued stationary state and its instability of the transmitted light by a ring cavity system," *Optics Communications*, vol. 30, no. 2, pp. 257–261, 1979.

[73] V. Torres-Company, D. Castelló-Lurbe, and E. Silvestre, "Comparative analysis of spectral coherence in microresonator frequency combs," *Optics Express*, vol. 22, no. 4, pp. 4678–4691, 2014.

[74] J. M. Dudley and S. Coen, "Coherence properties of supercontinuum spectra generated in photonic crystal and tapered optical fibers," *Optics Letters*, vol. 27, no. 13, pp. 1180–1182, 2002.

[75] L. A. Lugiato and R. Lefever, "Spatial Dissipative Structures in Passive Optical Systems," *Physical Review Letters*, vol. 58, no. 21, pp. 2209–2211, 1987.

[76] M. Haelterman, S. Trillo, and S. Wabnitz, "Dissipative modulation instability in a nonlinear dispersive ring cavity," *Optics Communications*, vol. 91, no. 5-6, pp. 401–407, 1992.

[77] I. V. Barashenkov and Y. S. Smirnov, "Existence and stability chart for the ac-driven, damped nonlinear Schrödinger solitons," *Physical Review E*, vol. 54, no. 5, pp. 5707–5725, 1996.

[78] C. Godey, I. V. Balakireva, A. Coillet, and Y. K. Chembo, "Stability analysis of the spatiotemporal Lugiato-Lefever model for Kerr optical frequency combs in the anomalous and normal dispersion regimes," *Physical Review A*, vol. 89, no. 6, p. 063814, 2014.

[79] P. Parra-Rivas, E. Knobloch, D. Gomila, and L. Gelens, "Dark solitons in the Lugiato-Lefever equation with normal dispersion," *Physical Review A*, vol. 93, no. 6, p. 063839, 2016.

[80] T. Hansson, D. Modotto, and S. Wabnitz, "Dynamics of the modulational instability in microresonator frequency combs," *Physical Review A*, vol. 88, no. 2, p. 023819, 2013.

[81] S. Coen and M. Erkintalo, "Universal scaling laws of Kerr frequency combs," *Optics Letters*, vol. 38, no. 11, pp. 1790–1792, 2013.

[82] T. J. Kippenberg, S. M. Spillane, and K. J. Vahala, "Kerr-Nonlinearity Optical Parametric Oscillation in an Ultrahigh-Q Toroid Microcavity," *Physical Review Letters*, vol. 93, no. 8, p. 083904, 2004.

[83] A. Coillet and Y. Chembo, "On the robustness of phase locking in Kerr optical frequency combs," *Optics Letters*, vol. 39, no. 6, pp. 1529–1532, 2014.

[84] M. R. E. Lamont, Y. Okawachi, and A. L. Gaeta, "Route to stabilized ultrabroadband microresonator-based frequency combs," *Optics Letters*, vol. 38, no. 18, pp. 3478–3481, 2013.

[85] J. A. Jaramillo-Villegas, X. Xue, P.-H. Wang, D. E. Leaird, and A. M. Weiner, "Deterministic single soliton generation and compression in microring resonators avoiding the chaotic region," *Optics Express*, vol. 23, no. 8, pp. 9618–9626, 2015.

[86] Y. Liu, Y. Xuan, X. Xue, P.-H. Wang, S. Chen, A. J. Metcalf, J. Wang, D. E. Leaird, M. Qi, and A. M. Weiner, "Investigation of mode coupling in normal-dispersion silicon nitride microresonators for Kerr frequency comb generation," *Optica*, vol. 1, no. 3, pp. 137–144, 2014.

[87] J. K. Jang, Y. Okawachi, M. Yu, K. Luke, X. Ji, M. Lipson, and A. L. Gaeta, "Dynamics of mode-coupling-induced microresonator frequency combs in normal dispersion," *Optics Express*, vol. 24, no. 25, pp. 28 794–28 803, 2016.

[88] A. B. Matsko, A. A. Savchenkov, D. Strekalov, V. S. Ilchenko, and L. Maleki, "Optical hyperparametric oscillations in a whispering-gallery-mode resonator: Threshold and phase diffusion," *Physical Review A*, vol. 71, no. 3, p. 033804, 2005.

[89] S. Wabnitz, "Suppression of interactions in a phase-locked soliton optical memory," *Optics Letters*, vol. 18, no. 8, pp. 601–603, 1993.

[90] C. Joshi, J. K. Jang, K. Luke, X. Ji, S. A. Miller, A. Klenner, Y. Okawachi, M. Lipson, and A. L. Gaeta, "Thermally controlled comb generation and soliton modelocking in microresonators," *Optics Letters*, vol. 41, no. 11, pp. 2565–2568, 2016.

[91] J. Liu, E. Lucas, A. S. Raja, J. He, J. Riemensberger, R. N. Wang, M. Karpov, H. Guo, R. Bouchand, and T. J. Kippenberg, "Photonic microwave generation in the X- and K-band using integrated soliton microcombs," *Nature Photonics*, vol. 14, no. 8, pp. 486–491, 2020.

[92] P. Trocha, M. Karpov, D. Ganin, M. H. P. Pfeiffer, A. Kordts, S. Wolf, J. Krockenberger, P. Marin-Palomo, C. Weimann, S. Randel, W. Freude, T. J. Kippenberg, and C. Koos, "Ultrafast optical ranging using microresonator soliton frequency combs," *Science*, vol. 359, no. 6378, pp. 887–891, 2018.

[93] M.-G. Suh, X. Yi, Y.-H. Lai, S. Leifer, I. S. Grudinin, G. Vasisht, E. C. Martin, M. P. Fitzgerald, G. Doppmann, J. Wang, D. Mawet, S. B. Papp, S. A. Diddams, C. Beichman, and K. Vahala, "Searching for exoplanets using a microresonator astrocomb," *Nature Photonics*, vol. 13, no. 1, pp. 25–30, 2019.

[94] Z. L. Newman, V. Maurice, T. Drake, J. R. Stone, T. C. Briles, D. T. Spencer, C. Fredrick, Q. Li, D. Westly, B. R. Ilic, B. Shen, M.-G. Suh, K. Y. Yang, C. Johnson, D. M. S. Johnson, L. Hollberg, K. J. Vahala, K. Srinivasan, S. A. Diddams, J. Kitching, S. B. Papp, and M. T. Hummon, "Architecture for the photonic integration of an optical atomic clock," *Optica*, vol. 6, no. 5, pp. 680–685, 2019.

[95] A. V. Cherenkov, V. E. Lobanov, and M. L. Gorodetsky, "Dissipative Kerr solitons and Cherenkov radiation in optical microresonators with third-order dispersion," *Physical Review A*, vol. 95, no. 3, p. 033810, 2017.

[96] X. Xue, X. Zheng, and B. Zhou, "Super-efficient temporal solitons in mutually coupled optical cavities," *Nature Photonics*, vol. 13, no. 9, pp. 616–622, 2019.

[97] P. Parra-Rivas, D. Gomila, E. Knobloch, S. Coen, and L. Gelens, "Origin and stability of dark pulse Kerr combs in normal dispersion resonators," *Optics Letters*, vol. 41, no. 11, pp. 2402–2405, 2016.

[98] S. Coen, M. Tlidi, P. Emplit, and M. Haelterman, "Convection versus Dispersion in Optical Bistability," *Physical Review Letters*, vol. 83, no. 12, pp. 2328–2331, 1999.

[99] W. Liang, A. A. Savchenkov, V. S. Ilchenko, D. Eliyahu, D. Seidel, A. B. Matsko, and L. Maleki, "Generation of a coherent near-infrared Kerr frequency comb in a monolithic microresonator with normal GVD," *Optics Letters*, vol. 39, no. 10, pp. 2920–2923, 2014.

[100] S. Fujii, Y. Okabe, R. Suzuki, T. Kato, A. Hori, Y. Honda, and T. Tanabe, "Analysis of Mode Coupling Assisted Kerr Comb Generation in Normal Dispersion System," *IEEE Photonics Journal*, vol. 10, no. 5, p. 4501511, 2018.

[101] V. Lobanov, G. Lihachev, T. J. Kippenberg, and M. Gorodetsky, "Frequency combs and platicons in optical microresonators with normal GVD," *Optics Express*, vol. 23, no. 6, pp. 7713–7721, 2015.